Molecular optical imaging probes for early diagnosis of drug-induced acute kidney injury

Huang, Jiaguo; Li, Jingchao; Lyu, Yan; Miao, Qingqing; Pu, Kanyi

2019

https://hdl.handle.net/10356/82606

https://doi.org/10.1038/s41563-019-0378-4

Molecular Optical Imaging Probes for Early Diagnosis of Drug-Induced Acute Kidney Injury

Jiaguo Huang, Jingchao Li, Yan Lyu, Qingqing Miao, and Kanyi Pu*

School of Chemical and Biomedical Engineering, Nanyang Technological University, Singapore, 637457

*E-mail: kypu@ntu.edu.sg

Abstract. Drug-induced acute kidney injury (AKI) with a high morbidity and mortality is poorly diagnosed in hospitals and deficiently evaluated in drug discovery. Here, we report the development of molecular renal probes (MRPs) with a record high renal clearance efficiency for in vivo optical imaging of drug-induced AKI. MRPs specifically activates their near-infrared fluorescence or chemiluminescence signals towards the prodromal biomarkers of AKI including superoxide anion, N-acetyl-β-D-glucosaminidase and caspase-3, enabling the first example of longitudinal imaging of multiple molecular events in the kidneys of living mice. Importantly, they in situ report the sequential occurrence of oxidative stress, lysosomal damage and cellular apoptosis, which precedes clinical manifestation of AKI (decreased glomerular filtration). Such an active imaging mechanism allows MRPs to noninvasively detect the onset of cisplatin-induced AKI at least 36 h earlier than the existing imaging methods. MRPs can also act as exogenous tracers for optical urinalysis that outperforms typical clinical/preclinical assays, demonstrating their clinical promise for early diagnosis of AKI.

Acute kidney injury (AKI) manifests as a rapid decline in renal function and is a significant health issue including a high morbidity and mortality with an estimated 1.7 million deaths per year globally[1]. The main etiologies of AKI include sepsis, ischemia/reperfusion, and nephrotoxin exposure[2, 3]. Among them, nephrotoxicity underlies up to 25% of AKI cases due to the use of clinically approved drugs[4]. The morbidity of drug-induced AKI can be reduced via a safer pharmacopeia and/or close monitoring of renal function during the use of known nephrotoxic drugs[5]. Particularly, early detection of kidney injury at the incipient stage can allow renoprotective intervention to be timely conducted to prevent AKI from progression into severer complications including chronic kidney disease (CKD), renal replacement therapy (RRT), and death, and aid in kidney recovery[6]. However, drug-induced AKI is deficiently evaluated in drug discovery due to the limitations of in vitro assays[5]. Moreover, current clinical diagnostic methods cannot identify AKI early because they often rely on the measurement of serum creatinine (sCr) and blood urea nitrogen (BUN)[7], which are insensitive indicators of late-stage renal dysfunction[8]. Therefore, drug-induced AKI will likely remain a clinical inevitability due to the increased use of prescription drugs and aggressive pharmaco-medical management[9].

Molecular imaging is a noninvasive way to detect the onset and progression of diseases in real-time in living organisms[10-13]. It has promise for *in situ* longitudinal monitoring of molecular events in kidneys, which is difficult for *in vitro* diagnostic methods based on the static analysis. While single photon emission computed tomography (SPECT), contrast-enhanced computed tomography (CT), magnetic resonance imaging (MRI) and ultrasonography are used routinely for kidney imaging, they mainly detect anatomic and functional changes of organs and have little utility in detecting the early-stage molecular-level changes that underlie AKI[14]. In contrast, optical imaging offers high spatiotemporal resolution and superb sensitivity[15-18] and can measure subtle changes in biomarker concentrations at the disease site via molecular probes[19, 20]. However, real-time in vivo optical imaging of drug-induced AKI has yet to be revealed.

Identification of early biomarkers and development of related molecular probes are crucial for early diagnosis of drug-induced AKI. Previously, the lysosomal enzyme (*N*-acetyl-beta-*D*-glucosaminidase [NAG])[21], inflammatory mediators (trefoil factor-3 [TFF3][22], osteopontin [OPN][23] and neutrophil gelatinase-associated lipocalin [NGAL][24]), glomerular filtration markers (cystatin-C [Cyst C][24] and β2-Microglobulin [β2-Mic][24]), and other upregulated structural proteins (kidney injury molecule-1 [KIM-1][21] and clusterin [Clust][24]) were qualified by the Food and Drug Administration (FDA) as safety biomarkers for detection of kidney injury. In addition, reactive oxygen species (ROS) has been well reported to be associated with AKI, and dysregulation of ROS can trigger the pathways towards lysosomal

damage, cellular apoptosis, necrosis, and renal fibrosis[25]. Moreover, many *in vitro* reports have shown that ROS-induced byproducts (isoprostanes, malondialdehyde, and oxidized proteins et al.) [26] and inflammatory mediators (NGAL, OPN, and interleukin-18 [IL-18] et al.) are dysregulated in plasma/urine prior to a substantial increase in sCr/BUN[27]. The fact that both ROS-induced byproducts and inflammatory mediators are generated at the downstream of oxidative stress implies that direct ROS detection could identify AKI earlier.

We report here the development of optical molecular renal probes (MRPs) for real-time imaging of early-stage biomarkers in the murine models of drug-induced AKI. These probes comprise three key building blocks (**Fig. 1**): renal clearance moiety, biomarker reactive moiety, and luminescent signaling moiety. Molecular screening found that (2-hydroxypropyl)-β-cyclodextrin (HPβCD) could dramatically facilitate probe renal clearance with the efficacy above 97%. Superoxide anion ($O_2^{\cdot-}$), NAG, and caspase-3 are selected as the target AKI biomarkers because they are related to oxidative stress, lysosomal damage, and cellular apoptosis, respectively. MRPs1-3 (**Fig. 1**) are single-channel probes that turn-on their near-infrared fluorescence (NIRF) in the presence of these three respective biomarkers. MRP$_D$ (**Fig. 1**) is a dual-channel probe that is always fluorescent but only becomes chemiluminescent after reaction with $O_2^{\cdot-}$. The fluorescent MRPs offer imaging of three interlinked molecular events in the kidneys to identify the earliest predictor for AKI. The MRP$_D$ enables simultaneous monitoring of $O_2^{\cdot-}$ and probe clearance via the chemiluminescent and NIRF signals, respectively, providing the feasibility to directly compare the time between upregulation of $O_2^{\cdot-}$ and changes in glomerular filtration after nephrotoxic exposure in living animals.

Synthesis and In Vitro Detection

MRPs were synthesized via a convergent approach (Supplementary **Fig. 1&2**). The fluorescent MRPs (MRPs1-3) were constructed on a hemi-cyanine precursor (CyOH) with an aromatic hydroxyl group and an azide group on the alky chain linked to the indole ring (Supplementary **Fig. 1** and Methods). The hydroxyl group of CyOH was first caged with diphenylphosphinyl, *N*-acetyl-*β*-*D*-glucosaminide, or a tetrapeptide sequence (Asp-Glu-Val-Asp: Ac-DEVD) (Supplementary **Fig. 3** and Methods), which could be specifically cleaved by $O_2^{\cdot-}$, NAG and caspase-3, respectively. The azide group of CyOH was then conjugated with the alkyne-functionalized HPβCD *via* a click reaction. MRP$_D$ was synthesized from an uncaged fluorescent heptamethine cyanine dye (Cy7NH2) (Supplementary **Fig. 2** and Methods), which has two azide groups on the alky chain linked to the indole ring and an alkyl amine on the *meso* position. The amine group of Cy7NH2 was first coupled with the caged chemiluminescent phenoxy-dioxetane substrate stabilized by a $O_2^{\cdot-}$-cleavable

trifluoromethanesulfonate group on the phenol position. The azide groups were then reacted with the alkyne-functionalized HPβCD to afford MRP$_D$.

MRPs1-3 had similar optical profiles with an absorption maximum at ~600 nm and were barely fluorescent at the intrinsic state (**Fig. 2a-c**). This was because they were "caged" wherein the electron-donating ability of the aromatic hydroxyl group was inhibited by the substituents[28]. The absorption spectra of MRPs1-3 changed in respond to their respective biomarkers with a peak shift to 695 nm; meanwhile, the fluorescence at 720 nm (**Fig. 2e-g**) increased by 21, 19, and 17-fold for MRP1, MRP2, and MRP3, respectively. The optical profiles of these probes resembled the uncaged derivative (CCD) (Supplementary **Fig. 4a**), which had an unsubstituted hydroxyl group liberating the strong electron-donating ability of the phenolate group on the fluorophores. High-performance liquid chromatography (HPLC) analysis (Supplementary **Fig. 4**) confirmed the rapid cleavage of the responsive moieties in MRPs1-3 by their respective biomarkers. The limit of detection (LOD) for MRP1 against $O_2^{\cdot-}$ was 11 nM (Supplementary **Fig. 4b-d**); the catalytic efficiencies (K_{cat}/K_m) of NAG towards MRP2 (and caspase-3 towards MRP3) were calculated to be 0.17 and 0.86 μM^{-1} s^{-1}, respectively (Supplementary **Fig. 4e-f and Table 1**). In contrast, the fluorescence intensities of MRPs1-3 only showed neglectable fluorescence increases towards the interfering substances including other enzymes, ROS, and metal ions (**Fig. 2i-k**), confirming their high specificity.

In contrast to the turn-on fluorescent response of MRPs1-3, the fluorescence of MRP$_D$ was always on and inert to the tested biological molecules (**Fig. 2d**). MRP$_D$ had a chemiluminescent phenoxy-dioxetane unit whose activity was initially inhibited due to the presence of trifluoromethanesulfonate substitution on its phenol group. In the presence of $O_2^{\cdot-}$, nucleophilic attack occurred on the sulfonate ester group of MRP$_D$, leading to the cleavage of trifluoromethanesulfonate and formation of a phenolate dioxetane intermediate (Supplementary **Fig. 5**). This unprotected intermediate was unstable and spontaneously underwent a chemically initiated electron-exchange luminescence process[29], resulting in the chemiluminescence at 540 nm. Addition of $O_2^{\cdot-}$ to MRP$_D$ led to a 3000-fold increase in chemiluminescent signal (**Fig. 2h**), which was not observed with other substances (**Fig. 2l**). The LOD for MRP$_D$ against $O_2^{\cdot-}$ (13 nM) was similar to MRP1, and its chemiluminescence half-life (8.9 min) was sufficient for in vivo imaging (Supplementary **Fig. 6**). Note that despite the presence of the NIR-emissive unit in MRP$_D$, the chemiluminescence maximum was the same as the dioxetane unit itself (540 nm) suggesting little energy transfer between the chemiluminescent unit and the NIR unit probably because of their long distance. This chemiluminescence was detected through 1.5 cm of chicken tissue (Supplementary **Fig. 6e-h**), confirming its utility for in vivo imaging.

Renal Clearance and In Vivo Stability Studies

The biodistribution of MRPs was studied and compared with their uncaged derivatives including the methyl-substituted hemicyanine skeleton (CMe), the HPβCD-substituted CyOH (CCD), and the poly(ethylene glycol) (PEG) substituted CyOH (CP2 and CP5 with PEG2000 and PEG5000, respectively) (**Fig. 3a**). Because the uncaged derivatives and MRP$_D$ were intrinsically fluorescent (Supplementary **Table 2**), NIRF imaging was used to track their biodistribution after intravenous (i.v.) administration. Fluorescence signals were quickly detected for CCD and MRP$_D$ in the kidneys and bladder 30 min post-injection (Supplementary **Fig. 7a**); this was not seen for CP2, CP5 and CMe in the whole-body images.

Ex vivo NIRF imaging of the abdominal cavity of mice (**Fig. 3b**) and biodistribution data (Supplementary **Fig. 7b-c**) at 1 h post-injection showed that CCD and MRP$_D$ mainly accumulated in the kidneys and bladder. The signals in other organs were close to the background of saline-treated mice. In contrast, CP2 and CP5 had a relatively high accumulation in gallbladder, liver, lung and muscle in addition to kidneys and bladder; CMe was trapped by the reticuloendothelial system (RES) and mainly accumulated in the liver, gallbladder, and intestine. Thus, the ex vivo data revealed that although both PEG and HPβCD-substituted CyOH could be excreted through the kidney, the relatively high uptake in other organs for CP2 and CP5 caused signal interference limiting kidney visualization in the real-time whole-body images.

HPLC was used to study fluorophore pharmacokinetics by quantifying the fluorophores in the blood and urine of living mice as a function of time after i.v. injection. The probe concentration in blood decreased close to 0 % injected doses (ID) g^{-1} 75 min post-injection for all fluorophores (**Fig. 3c**). The elimination half-lives (t$_{1/2β}$) of the HPβCD-substituted fluorophores (<17 min) were shorter than CP2 (20.8 min) (Supplementary **Table. 3**). Furthermore, the trend of t$_{1/2β}$ was generally consistent with their distribution coefficients (Log D) (**Fig. 3d**), implying that hydrophilicity played a role in their blood elimination. Urine analysis showed that the renal clearance efficiencies of the HPβCD-substituted fluorophores were higher than others (**Fig. 3e** and Supplementary **Fig. 8**). These were determined to be >80% ID at 3 h post-injection and >92% ID at 24 h post-injection (92±2.1, 94±2.2, 93±2.0, 94±3.0 and 97±2.7% ID for MRP1, MRP2, MRR3, MRP$_D$, and CCD, respectively). In contrast, CP2 and CP5 only reached 79±3 and 55±5% ID at 24 h post-injection, respectively, and CMe was nearly undetectable in urine due to RES uptake. The highly efficient renal clearance of MRPs is attributed to their relatively low molecular weights (<50 kDa, below glomerular filtration cutoff) and high hydrophilicity.

To determine in vivo stability, the optical and chemical profiles of MRPs recovered from the urine of living mice were measured and compared with the pure compounds. Except CMe (unable to be recovered from urine), none of fluorophores from urine had obvious changes to their absorption and fluorescence spectra after circulation in living mice (Supplementary **Fig. 9**). Although matrix assisted laser desorption/ionization (MALDI) analysis validated their intact chemical structures (Supplementary **Fig. 10**), HPLC quantification (**Fig. 3f**) identified some CCDs and adamantanone (<6%) from the urine of MRPs1-3 and MRP$_D$-treated mice, respectively. This is likely due to probe activation by basal levels of biomarkers in healthy mice. These data not only showed that MRPs had minimal in vivo metabolism in healthy mice but also confirmed that their renal clearance efficiencies were near 100% ID for MRPs. In view of the undetectable signals in the major organs at 24 h post-injection of MRPs (Supplementary **Fig. 8j&l**), MRPs could be considered as fully renal clearable (>97% ID). In addition, histological and immunofluorescence staining revealed that MRPs did not induce cellular apoptosis or cause any tissue damage (Supplementary **Fig. 11**).

Real-time NIRF Imaging

The ability of MRPs1-3 to detect drug-induced AKI was tested in living mice treated with cisplatin (an antineoplastic drug), gentamicin (an antibiotic), or diatrizoate (a radiocontrast agent)—all with known nephrotoxicity[30-32]. Cisplatin was intraperitoneally administered into living mice at a nephrotoxic dosage (**Fig. 4a** and Methods), followed by intravenous injection of MRPs at different timepoints post-treatment of cisplatin (8, 12, 16, 24, and 48 h). The control groups were treated with saline or a nephroprotective antioxidant (NAC) prior to cisplatin administration. Longitudinal NIRF imaging was then conducted for those groups with different drug post-treatment times. At 8 h post-treatment of cisplatin, the signals from MRPs1-3 in the kidneys were as low as the control mice (**Fig. 4b-d** and Supplementary **Fig. 12**). However, at 12 h post-treatment of cisplatin, the injection of MRP1 led to a gradual signal increase in the kidneys with a signal maximum 30 min post-injection of MRP1 (**Fig. 4e**; 1.45-fold higher than control mice). The MRP1 signals in the kidneys and bladder decreased at later imaging timepoints due to its short elimination half-life. Similar trends were observed for MRP2 and MRP3, but the earliest timepoints that they showed a statistically significant signal increase were 16 and 48 h post-treatment of cisplatin for MRP2 (1.56-fold) and MRP3 (1.60-fold), respectively (**Fig. 4f** and Supplementary **Fig. 12**). This sequential activation suggested that cisplatin first induced oxidative stress followed by lysosomal damage and cellular apoptosis. The maximum NIRF signals of MRPs1-2 in the kidneys increased with post drug treatment time (**Fig. 4f**), indicating the gradual upregulation of those biomarkers during the progression of AKI.

Consistent with the in vivo imaging data, whole kidney section imaging revealed that the NIRF signals (**Fig. 4g** and Supplementary **Fig. 13**) were detected in the cortex and the outer medulla area for MRP1, MRP2, and MRP3 at 12, 16 and 48 h post-treatment of cisplatin, respectively. The caspase-3 signal was only detectable 48 h post-treatment of cisplatin, and the histological staining (**Fig. 4h** and Supplementary **Fig. 13k**) showed normal tubular morphology at 48 h post-treatment of cisplatin, but loss of the brush border and hyaline casts at 72 h post-treatment of cisplatin. Magnified regional kidney section imaging further clarified that the NIRF signals of activated MRPs1-3 mainly came from the renal tubules rather than the glomeruli (**Fig. 4i**). This was because the tubules are at the frontline of nephrotoxin clearance; tubular injury is well reported for nephrotoxin exposure[33]. Thus, these data further validated that $O_2^{\cdot-}$, NAG, and caspase-3 were sequentially upregulated prior to injury of kidney tissue. It also revealed that these molecular events occurred in renal tubules after nephrotoxin exposure. Note that similar trends were observed for the signal increases of MRPs1-2 in the mouse model of gentamicin or diatrizoate-induced AKI (Supplementary **Fig. 14-17**).

Real-time Independent Dual-Channel Imaging

To confirm that MRPs could predict drug-induced AKI before the change in glomerular filtration, the dual-channel probe (MRP$_D$) was intravenously injected into living mice at different post drug treatment time (8, 12, 48 and 72 h). Longitudinal chemiluminescence and NIRF imaging were simultaneously conducted. At 8 h post-treatment of cisplatin, the chemiluminescent signal of MRP$_D$ in the kidneys was close to the background (**Fig. 5a** and Supplementary **Fig. 18**), but the NIRF signal was detected (**Fig. 5b**; always-on signal). The NIRF signal reached maximum at 8 min post-injection of MRP$_D$ and then decreased with time (**Fig. 5e**). At 12 h post-treatment of cisplatin, the chemiluminescent signal was detected in the kidney, 14.6-fold higher than that of the control at 8 min post-injection of MRP$_D$. Moreover, similar chemiluminescent signal evaluation as a function of imaging time was observed for the mice groups at 12, 48 and 72 h post-treatment of cisplatin (**Fig. 5d**); however, the maximum chemiluminescent signal of the kidneys at 72 h post-treatment of cisplatin was 1.27 and 1.66-fold higher than that at 48 and 12 h, respectively. This proportional correlation between the maximum chemiluminescent signal and the post-treatment time was consistent with the data acquired with MRP1, confirming that the level of $O_2^{\cdot-}$ was gradually upregulated after drug treatment. In contrast, the maximum NIRF signals of the kidneys had a non-linear relation with post-treatment time, and a threshold was observed. The profile for the signal as a function of imaging time remained similar when the post-treatment time was no more than 48 h; it changed dramatically at 72 h post-treatment.

Instead of gradually decreasing signal 8 min after injection of MRP_D, the signal was stable, indicating the probe retention in the kidneys.

To gain insight into the origin of probe retention in the kidneys, the pharmacokinetics of MRP_D (**Fig. 5f**) and GFR (**Fig. 5c**) were measured in the mice at different timepoints post-treatment of cisplatin. The blood elimination half-lives ($t_{1/2\beta}$) of MRP_D in the mice after cisplatin treatment for 8, 12, and 48 h were similar (14.3 min), but it prolonged to 34.7 min for 72 h. This was ascribed to the significantly decreased GFR from 9.78 before treatment to 4.50 µl min^{-1} g^{-1} body weight at 72 h post-treatment. Thus, these data further proved that the probe retention was caused by declined glomerular filtration capability under nephrotoxic expose, consistent with the histological data showing renal tubular damage (Supplementary **Fig. 13**). Moreover, the fact that the chemiluminescent signal of MRP_D was detected at 12 h before the decrease in GFR indicated the ability of MRP_D for early detection of drug-induced AKI. Similar trends of dual-channel imaging results and GFR changes were observed for MRP_D in the mouse model of gentamicin or diatrizoate induced AKI (Supplementary **Fig. 19-21**).

In Vitro Diagnosis

To evaluate the translational potential of MRPs, drug-induced AKI was detected in urine and compared with existing assays. Two methods were used for MRP-based urinalysis (**Fig. 6a**): (i) direct NIRF measurement of excreted probes in urine after their intravenous injection into drug-treated mice (online urinalysis) and (ii) collection of urine samples from drug-treated mice followed by probe incubation and optical measurement (offline urinalysis). In online urinalysis (**Fig. 6b-d** and Supplementary **Fig. 22&23**), the first statistically significant NIRF enhancement was respectively observed at 12 (2.0-fold), 36 (2.3-fold), and 8 h (2.1-fold) post-treatment of cisplatin, gentamicin, and diatrizoate for excreted MRP1, 16 (2.3-fold), 48 (2.3-fold) and 16 h (2.4-fold) for MRP2, and 48 (2.6-fold), 144 (2.8-fold) and 24 h (1.9-fold) for MRP3. Moreover, the NIRF signal continued increasing after these timepoints. The signal evolution behaviors of MRPs coincided with the real-time NIRF imaging data, as the excreted MRPs were activated in the renal clearance pathway. In offline urinalysis (**Fig. 6e-g** and Supplementary **Fig. 23**), only MRP2 showed statistically significant NIRF enhancement after incubation in urine because $O_2^{\cdot-}$ has a short half-life (< 5 s)[34], and caspase-3 is an intracellular enzyme that is excreted less in urine[35]. The earliest timepoints for MRP2 to detect the upregulation of NAG in offline urinalysis were 24 (2.7-fold), 72 (2.1-fold) and 24 (2.7-fold) for cisplatin-, gentamicin-, and diatrizoate-treated mice, respectively. These were slightly later (8-24 h) than those in online urinalysis, probably due to the diluted concentration of NAG in the urine relative to the kidneys.

Commercial assays were used to measure sCr, BUN, and Cystatin C in blood as well as NGAL, clusterin, KIM-1, osteopontin, β2-microglobulin and trefoil factor-3 in urine. The sCr and BUN had the statistically significant increase at 72 (2.4, 2.0-fold), 144 (2.9, 2.4-fold) and 24 h (1.8, 2.0-fold) after treatment of cisplatin, gentamicin and diatrizoate, respectively (**Fig. 6h-j**). At these timepoints, the GFRs were decreased by ~50% (Supplementary **Fig. 21**). The serum Cystatin C behaved similarly in gentamicin and diatrizoate models but increased earlier at 48 h (2.0-fold) in cisplatin model. Among the tested urinary biomarkers, KIM-1 and clusterin were most sensitive, showing their first statistically significant increases at 24 (1.9, 4.1-fold), 72 (2.2, 3.5-fold) and 24 h (3.7, 3.0-fold) after treatment of cisplatin, gentamicin, and diatrizoate, respectively. However, the first statistically significant changes of NGAL and trefoil factor-3 were observed at 48 (2.7, 0.4-fold), 96 (2.0, 0.3-fold) and 24 h (2.3, 0.5-fold) post-treatment of cisplatin, gentamicin, and diatrizoate, respectively. The statistically significant changes of osteopontin and β2-microglobulin after treatment of cisplatin, gentamicin, and diatrizoate occurred even later: 72 (2.3-fold) (cisplatin), 144 (2.3-fold) (gentamicin) and 24 h (2.3-fold) (diatrizoate) for osteopontin, and 72 (3.9-fold) (cisplatin), 144 (3.2-fold) (gentamicin) and 48 h (3.6-fold) (diatrizoate) for β2-microglobulin.

Comparison of the urinal/plasma analysis data (**Fig. 6k-m**) revealed that the MRPs1-2 based online urinalysis of upregulated $O_2^{\cdot-}$/NAG was most sensitive to detect drug-induced AKI. The first statistically significant change of MRP1/MRP2 based online urinalysis detected drug-induced AKI at least 12/8 (cisplatin), 36/24 (gentamicin), and 16/8 h (diatrizoate) earlier than both MRP2-based offline urinalysis and KIM1- or clusterin-based urinalysis, and at least 36/32 (cisplatin), 60/48 (gentamicin) and 16/8 h (diatrizoate) earlier than the clinical methods and other tested preclinical assays.

Summary and Outlook

The fundamental limitation in molecular imaging of AKI is a lack of molecular probes that simultaneously possess high renal clearance efficiency and activatable signals specific to early AKI biomarkers. Upon substitution of HPβCD, MRPs1-3, MRP$_D$, and CCD had renal clearance efficiencies (>97% ID at 24 h post-injection) higher than all existing imaging agents regardless of their imaging modalities and compositions (Supplementary **Table 4**) such as gold nanocluster (52% ID)[36], quantum dots (75% ID)[37], silica Cornell dots (73%)[38], zwitterionic fluorophores (86% ID)[39]. Even in drug-treated mice, the renal clearance efficiencies of MRPs were >82% ID at 24 h post-injection (Supplementary **Fig. 24**). The nearly complete renal clearance allowed the HPβCD-substituted fluorophore (CCD) to clearly delineate both kidneys of living mice through entire imaging course (Supplementary **Fig. 7a**); in contrast, PEG-substituted CP2 and CP5 and other reported fluorophores failed to do so due to the signal interference from the fluorophore uptake by other organs[40].

The high sensing specificity and ideal in vivo stability of MRPs1-3 in association with their nearly same pharmacokinetics permitted the first longitudinal imaging of multiple biomarkers ($O_2^{\cdot-}$, NAG and caspase-3) in the kidneys of drug-treated living mice. The real-time imaging results from three representative nephrotoxic drugs (cisplatin, gentamicin and diatrizoate) consistently showed that oxidative stress, lysosomal damage, and cellular apoptosis were prodromal molecular events occurring sequentially after nephrotoxic exposure. In comparison with the fluorescent turn-on probe (MRP1), MRP$_D$ sensed the upregulation of $O_2^{\cdot-}$ at the same timepoint but had a higher signal to background ratio (up 21-fold) due to minimized tissue autofluorescence in chemiluminescence imaging (Supplementary **Fig. 25**). Moreover, MRP$_D$ is the first probe of its kind with always-on fluorescence but biomarker-activated chemiluminescence[19, 41, 42]. Such an uncoordinated and intrinsically independent dual-channel imaging capability enabled MRP$_D$ to noninvasively validate that the chemiluminescence signal was activated by upregulated $O_2^{\cdot-}$ prior to the retention-caused enhancement of NIRF signals (**Fig. 5**).

Comparison of the detection timelines of MRPs with the changes in GFR after nephrotoxic exposure (**Fig. 6k-m**) directly proved that MRPs1-2 and MRP$_D$ detected AKI before a decrease in glomerular filtration. Particularly, MRPs1-3 sequentially detected upregulated $O_2^{\cdot-}$, NAG, and caspase-3 at 12, 16 and 48 h post-treatment in the cisplatin model of AKI. These timepoints were at least 36 h earlier than other real-time imaging methods based on the bioluminescent NGAL (168 h)[43] or transcription factor Nuclear factor erythroid 2-related factor 2 (Nrf2) (a major regulator responding to oxidative stress) (48 h) reporter genes[44] as well as the retention-based MRI, CT and SPECT contrast agents detecting the changes in glomerular filtration (>72 h)[14] in the mouse model with the same drug dosage (20 mg kg^{-1}) (Supplementary **Tables 5&6**). Such early detection capability of MRPs was also validated in other animal settings with the variation in drug dosages (Supplementary **Fig. 26-28**), mouse strains (Supplementary **Fig. 29-30**) and mouse ages (Supplementary **Fig. 31**). Thus, MRPs are by far the most sensitive probes that detect AKI at the incipient stage, which is imperative for timely initiation of renoprotective intervention to deter transition into severer complications and aid in recovery from AKI for hospitalized patients. Moreover, MRPs even could potentially detect drug-induced AKI on the backdrop of diabetes-related CKD (Supplementary **Fig. 32-33**), making them highly competent for drug development.

MRPs1-3 are promising for clinical diagnosis, because they are nontoxic and rapidly cleared renally. Although optical imaging has a relatively shallow imaging depth and thus is less suitable for real-time imaging of kidneys in patients, MRPs1-3 can act as exogenous tracers for optical urinalysis. In MRP-based online urinalysis, the signals of the excreted

probes were detected as early as the real-time imaging approach (**Fig. 6b-d** *vs* **Fig. 3b-d**)—these were again 16 to 108 h earlier than 50% decrease in GFR depending on the drugs. Additionally, the presence of urinary NAG allowed MRP2 to be valid for offline urinalysis simply by pre-incubation with mouse urine before optical analysis. Despite the slightly delayed detection timepoints relative to online urinalysis, MRP2-based offline urinalysis still outperformed most of the tested clinical assays and identified AKI 24-72 h earlier than the NAGL, Cyst C and β2-microglobulin assay (three assays better than sCr/BUN)[24] in a cisplatin- or gentamicin-induced AKI mouse model (**Fig. 6k**). Moreover, NAG has a molecular weight (140 kDa) larger than the glomerular filtration cutoff (50 kDa) ensuring that plasma NAG produced from other organs cannot be filtered through the glomerulus and excreted into urine[45]. Thereby, MRP2-based offline urinalysis should be specific to the AKI-induced renal NAG. Indeed, no signal enhancement was detected for MRP2 after incubation with urine from the mice with local inflammation (Supplementary **Fig. 34**) or liver injury (Supplementary **Fig. 35**).

In summary, we synthesized renal-clearable molecular probes for real-time optical imaging of sequential prodromal molecular events in the kidney of living mice undergoing nephrotoxic exposure. Such probes represent the first type of imaging agents that almost completely go through renal clearance, specifically react with the targeted biomarkers in kidneys, and spontaneously activate their optical signals to report abnormal upregulation at the incipient stage of drug-induced AKI before decrease in GFR. The ability of MRPs to be used as urinalysis tracers to detect drug-induced AKI earlier than current assays further underlines their potential in clinical translation. Our work thus opens up a molecular imaging approach that not only permits mechanistic investigation of nephrotoxicity and high-throughput drug screening in living animals, but also facilitates validation and translation of new biomarkers for diagnosis of kidney injury.

References

1. Chawla, L.S., Eggers, P.W., Star, R.A. & Kimmel, P.L. Acute kidney injury and chronic kidney disease as interconnected syndromes. *N. Engl. J. Med.* **371**, 58-66 (2014).
2. Abuelo, J.G. Normotensive ischemic acute renal failure. *N. Engl. J. Med.* **357**, 797-805 (2007).
3. Alobaidi, R., Basu, R.K., Goldstein, S.L. & Bagshaw, S.M. Sepsis-associated acute kidney injury. *Semin. Nephrol.* **35**, 2-11 (2015).
4. Kellum, J.A. & Prowle, J.R. Paradigms of acute kidney injury in the intensive care setting. *Nat. Rev. Nephrol.* **14**, 217-230 (2018).
5. Soo, J.Y.C., Jansen, J., Masereeuw, R. & Little, M.H. Advances in predictive in vitro models of drug-induced nephrotoxicity. *Nat. Rev. Nephrol.* **14**, 378-393 (2018).
6. Perazella, M.A. & Coca, S.G. Three feasible strategies to minimize kidney injury in 'incipient AKI'. *Nat. Rev. Nephrol.* **9**, 484-490 (2013).

7. Darmon, M. *et al*. Diagnostic work-up and specific causes of acute kidney injury. *Intensive Care. Med.* **43**, 829-840 (2017).

8. Wang, X. *et al*. Validation of creatinine-based estimates of GFR when evaluating risk factors in longitudinal studies of kidney disease. *J. Am. Soc. Nephrol.* **17**, 2900-2909 (2006).

9. Lameire, N.H. *et al*. Acute kidney injury: an increasing global concern. *The Lancet* **382**, 170-179 (2013).

10. Willmann, J.K., Van Bruggen, N., Dinkelborg, L.M. & Gambhir, S.S. Molecular imaging in drug development. *Nat. Rev. Drug Discov.* **7**, 591-607 (2008).

11. Miao, Q. *et al*. Molecular afterglow imaging with bright, biodegradable polymer nanoparticles. *Nat. Biotechnol.* **35**, 1102-1110 (2017).

12. Lovell, J.F. *et al*. Porphysome nanovesicles generated by porphyrin bilayers for use as multimodal biophotonic contrast agents. *Nat. Mater.* **10**, 324-332 (2011).

13. Ntziachristos, V., Ripoll, J., Wang, L.V. & Weissleder, R. Looking and listening to light: the evolution of whole-body photonic imaging. *Nat. Biotechnol.* **23**, 313-320 (2005).

14. Grenier, N., Merville, P. & Combe, C. Radiologic imaging of the renal parenchyma structure and function. *Nat. Rev. Nephrol.* **12**, 348-359 (2016).

15. Hong, G., Antaris, A.L. & Dai, H. Near-infrared fluorophores for biomedical imaging. *Nat. Biomed. Eng.* **1**, 0010 (2017).

16. So, M.K., Xu, C., Loening, A.M., Gambhir, S.S. & Rao, J. Self-illuminating quantum dot conjugates for in vivo imaging. *Nat. Biotechnol.* **24**, 339-343 (2006).

17. Smith, A.M., Mancini, M.C. & Nie, S. Bioimaging: second window for in vivo imaging. *Nat. Nanotechnol.* **4**, 710-711 (2009).

18. Ning, X. *et al*. Maltodextrin-based imaging probes detect bacteria in vivo with high sensitivity and specificity. *Nat. Mater.* **10**, 602-607 (2011).

19. Chan, J., Dodani, S.C. & Chang, C.J. Reaction-based small-molecule fluorescent probes for chemoselective bioimaging. *Nat. Chem.* **4**, 973-984 (2012).

20. Park, S.M., Aalipour, A., Vermesh, O., Yu, J.H. & Gambhir, S.S. Towards clinically translatable in vivo nanodiagnostics. *Nat. Rev. Mater.* **2**, 17014 (2017).

21. Vaidya, V.S. *et al*. Kidney injury molecule-1 outperforms traditional biomarkers of kidney injury in preclinical biomarker qualification studies. *Nat. Biotechnol.* **28**, 478-485 (2010).

22. Yu, Y. *et al*. Urinary biomarkers trefoil factor 3 and albumin enable early detection of kidney tubular injury. *Nat. Biotechnol.* **28**, 470-477 (2010).

23. Ozer, J.S. *et al*. A panel of urinary biomarkers to monitor reversibility of renal injury and a serum marker with improved potential to assess renal function. *Nat. Biotechnol.* **28**, 486-494 (2010).

24. Dieterle, F. *et al*. Urinary clusterin, cystatin C, β2-microglobulin and total protein as markers to detect drug-induced kidney injury. *Nat. Biotechnol.* **28**, 463-469 (2010).

25. Sureshbabu, A., Ryter, S.W. & Choi, M.E. Oxidative stress and autophagy: crucial modulators of kidney injury. *Redox Biol.* **4**, 208-214 (2015).

26. Ware, L.B., Fessel, J.P., May, A.K. & Roberts, L.J.2nd. Plasma biomarkers of oxidant stress and development of organ failure in severe sepsis. *Shock* **36**, 12-17 (2011).

27. Naud, J.F. & Leblanc, M. Biomarkers in acute kidney injury. *Kidney Int.* **3**, 115-125 (2008).

28. Miao, Q. *et al*. Near-infrared fluorescent molecular probe for sensitive imaging of keloid. *Angew. Chem. Int. Ed.* **57**, 1256-1260 (2018).

29. Hananya, N., Eldar Boock, A., Bauer, C.R., Satchi Fainaro, R. & Shabat, D. Remarkable enhancement of chemiluminescent signal by dioxetane-fluorophore conjugates: turn-on

chemiluminescence probes with color modulation for sensing and imaging. *J. Am. Chem. Soc.* **138**, 13438-13446 (2016).

30. Galgamuwa, R. *et al*. Dichloroacetate prevents cisplatin-induced nephrotoxicity without compromising cisplatin anticancer properties. *J. Am. Soc. Nephrol.* **27**, 3331-3344 (2016).

31. Otunctemur, A. *et al*. Protective effect of hydrogen sulfide on gentamicin-induced renal injury. *Ren. Fail.* **36**, 925-931 (2014).

32. Erley, C.M. *et al*. Prevention of radiocontrast-induced nephropathy by adenosine antagonists in rats with chronic nitric oxide deficiency. *J. Am. Soc. Nephrol.* **8**, 1125-1132 (1997).

33. Basile, D.P., Anderson, M.D. & Sutton, T.A. Pathophysiology of acute kidney injury. *Compr. Physiol.* **2**, 1303-1353 (2012).

34. Hayyan, M., Hashim, M.A. & AlNashef, I.M. Superoxide ion: generation and chemical implications. *Chem. Rev.* **116**, 3029-3085 (2016).

35. Zhivotovsky, B., Samali, A., Gahm, A. & Orrenius, S. Caspases: their intracellular localization and translocation during apoptosis. *Cell Death Differ.* **6**, 644-651 (1999).

36. Du, B. *et al*. Glomerular barrier behaves as an atomically precise bandpass filter in a sub-nanometre regime. *Nat. Nanotechnol.* **12**, 1096-1102 (2017).

37. Choi, H.S. *et al*. Renal clearance of quantum dots. *Nat. Biotechnol.* **25**, 1165-1170 (2007).

38. Burns, A.A. *et al*. Fluorescent silica nanoparticles with efficient urinary excretion for nanomedicine. *Nano Lett.* **9**, 442-448 (2009).

39. Owens, E.A., Henary, M., El Fakhri, G. & Choi, H.S. Tissue-specific near-infrared fluorescence imaging. *Acc. Chem. Res.* **49**, 1731-1740 (2016).

40. Antaris, A.L. *et al*. A small-molecule dye for NIR-II imaging. *Nat. Mater.* **15**, 235-242 (2016).

41. Dickinson, B.C. & Chang, C.J. Chemistry and biology of reactive oxygen species in signaling or stress responses. *Nat. Chem. Biol.* **7**, 504-511 (2011).

42. Shuhendler, A.J., Pu, K., Cui, L., Uetrecht, J.P. & Rao, J. Real-time imaging of oxidative and nitrosative stress in the liver of live animals for drug-toxicity testing. *Nat. Biotechnol.* **32**, 373-380 (2014).

43. Paragas, N. *et al*. The Ngal reporter mouse detects the response of the kidney to injury in real time. *Nat. Med.* **17**, 216-222 (2011).

44. Forootan, S.S. *et al*. Real-time in vivo imaging reveals localised Nrf2 stress responses associated with direct and metabolism-dependent drug toxicity. *Sci. Rep.* **7**, 16084 (2017).

45. Asami, T., Soichiro, O., Kasahara, T. & Uchiyama, M. Asymptomatic primary hyper-N-acetyl-beta-D-glucosaminidaseuria: a new clinical entity? *Pediatr. Nephrol.* **17**, 560-565 (2002).

Author contributions

K.P. and J.H. conceived and designed the study. J.H. and Q.M. performed the probes synthesis experiments. J.H. performed the in vivo experiments. J.H, J.L. and Y.L. performed the histology experiments. K.P. and J.H. contributed to the analysis and interpretation of results and the writing of the manuscript.

Competing financial interests

The authors declare no competing financial interests.

Data availability

The authors declare that all relevant data supporting the findings of this study are available within the article and in the Supplementary Information document, or from the corresponding author on reasonable request.
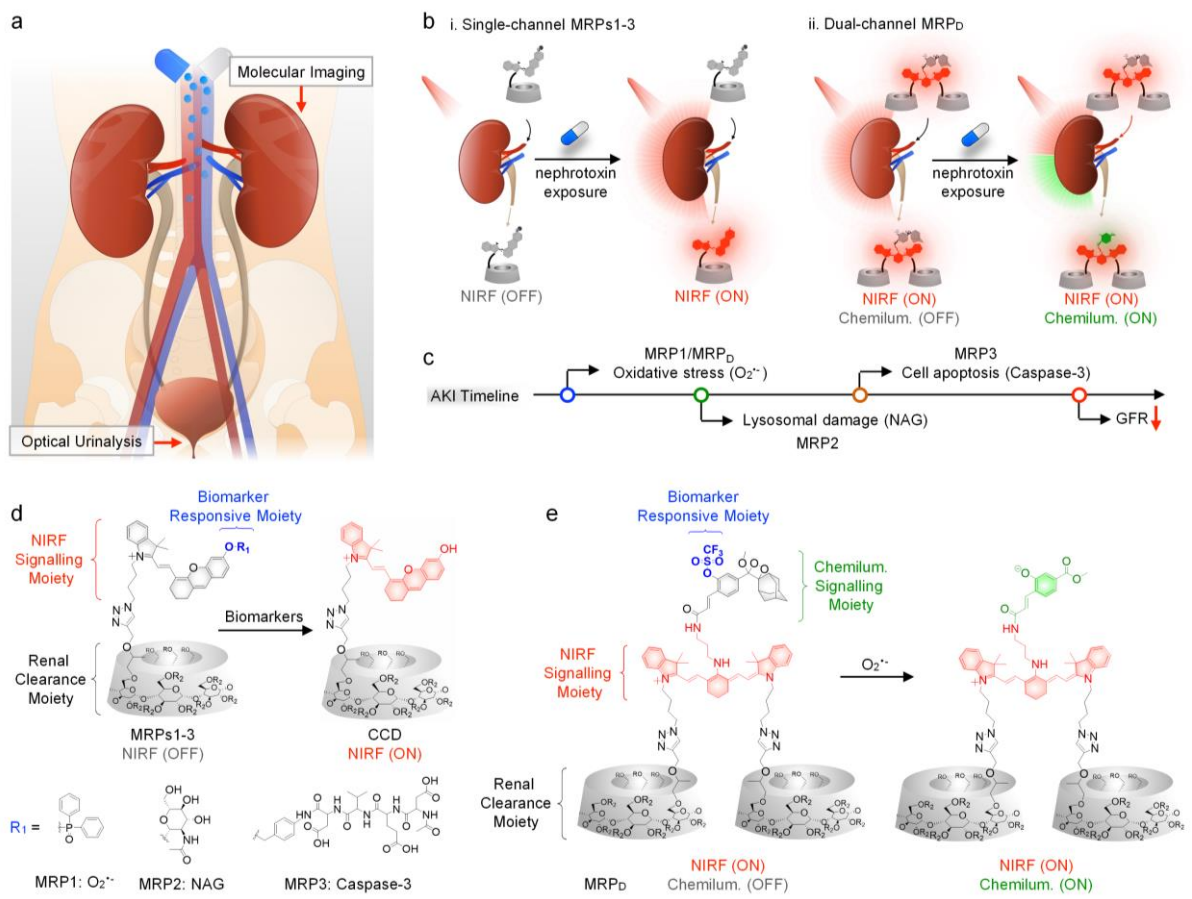
Fig 1. Design and mechanisms of MRPs for molecular imaging and early detection of drug-induced AKI. (**a**) Cartoon illustration of drug-induced AKI and AKI detection methods used here including molecular imaging and optical urinalysis. (**b**) Real-time noninvasive imaging of drug-induced AKI using single channel NIRF turn-on MRPs1-3 (i) and dual-channel chemiluminescent MRP_D (ii). (**c**) Timeline of AKI comparing the molecular events including oxidative stress, lysosomal damage and cell apoptosis with the decrease in glomerular filtration rate (GFR). (**d**) Chemical structures of MRPs1-3 and their activated form as CCD in response to their respective biomarkers ($O_2^{\bullet-}$ for MRP1, NAG for MRP2, and caspase-3 for MRP3). (**e**) Chemical structures of MRP_D and its activated form in response to $O_2^{\bullet-}$ (R_2 = H or $CH_2CHOHCH_3$).
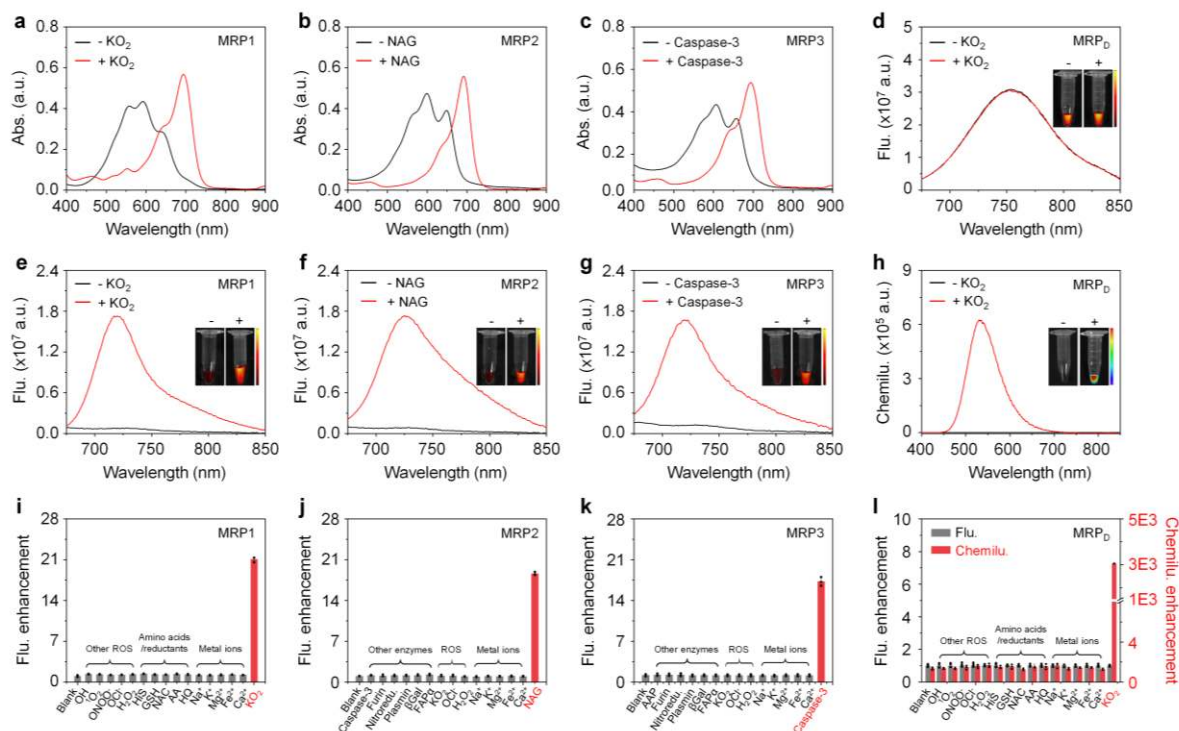
Fig. 2. In vitro evaluation of the MRPs sensing capabilities. UV-Vis absorption (**a-c**) and fluorescence spectra (**e-g**) of MRPs1-3 (30 µM) in the absence or presence of their respective biomarkers (60 µM KO$_2$, 40 mU NAG and 0.5 µg caspase-3, respectively) in PBS (10 mM, pH 7.4) at 37 °C. Fluorescence excitation at 675 nm. Inset: the corresponding fluorescence images acquired at 720 nm upon excitation at 675 nm with the IVIS spectrum imaging system. Fluorescence (**d**) and chemiluminescence spectra (**h**) of MRP$_D$ (30 µM) in the absence or presence of KO$_2$ (60 µM) in PBS (10 mM, pH 7.4) at 37 °C. Fluorescence excitation at 640 nm. Inset: the corresponding fluorescence images acquired at 760 nm upon excitation at 640 nm and chemiluminescence images acquired under bioluminescence mode with the acquisition time of 1 s. The experiments (a-h) were repeated independently three times with similar results. (**i-k**) The NIRF changes of MRPs1-3 (30 µM) at 720 nm after incubation with indicated ROS (150 µM), enzymes, and other analytes (150 µM in PBS (10 mM, pH 7.4) at 37 °C. (**l**) NIRF (760 nm) and chemiluminescence changes (540 nm) of MRP$_D$ (30 µM) after incubation with indicated ROS (150 µM) and other analytes (150 µM) in PBS (10 mM, pH 7.4) at 37 °C. Fluorescence excitation at 640 nm and chemiluminescence acquired under bioluminescence mode with the acquisition time of 1 s. Data are the mean ± SD. n = 3 independent experiments. Hydroxyl radical (•OH), peroxynitrite (ONOO$^-$), histidine (His), glutathione (GSH), N-acetyl-L-cysteine (NAC), ascorbic acid (AA), hydroquinone (HQ), nitroreductase (Nitroredu.), β-galactosidase (βGal), fibroblast activation protein-alpha (FAPα), alanine aminopeptidase (AAP).
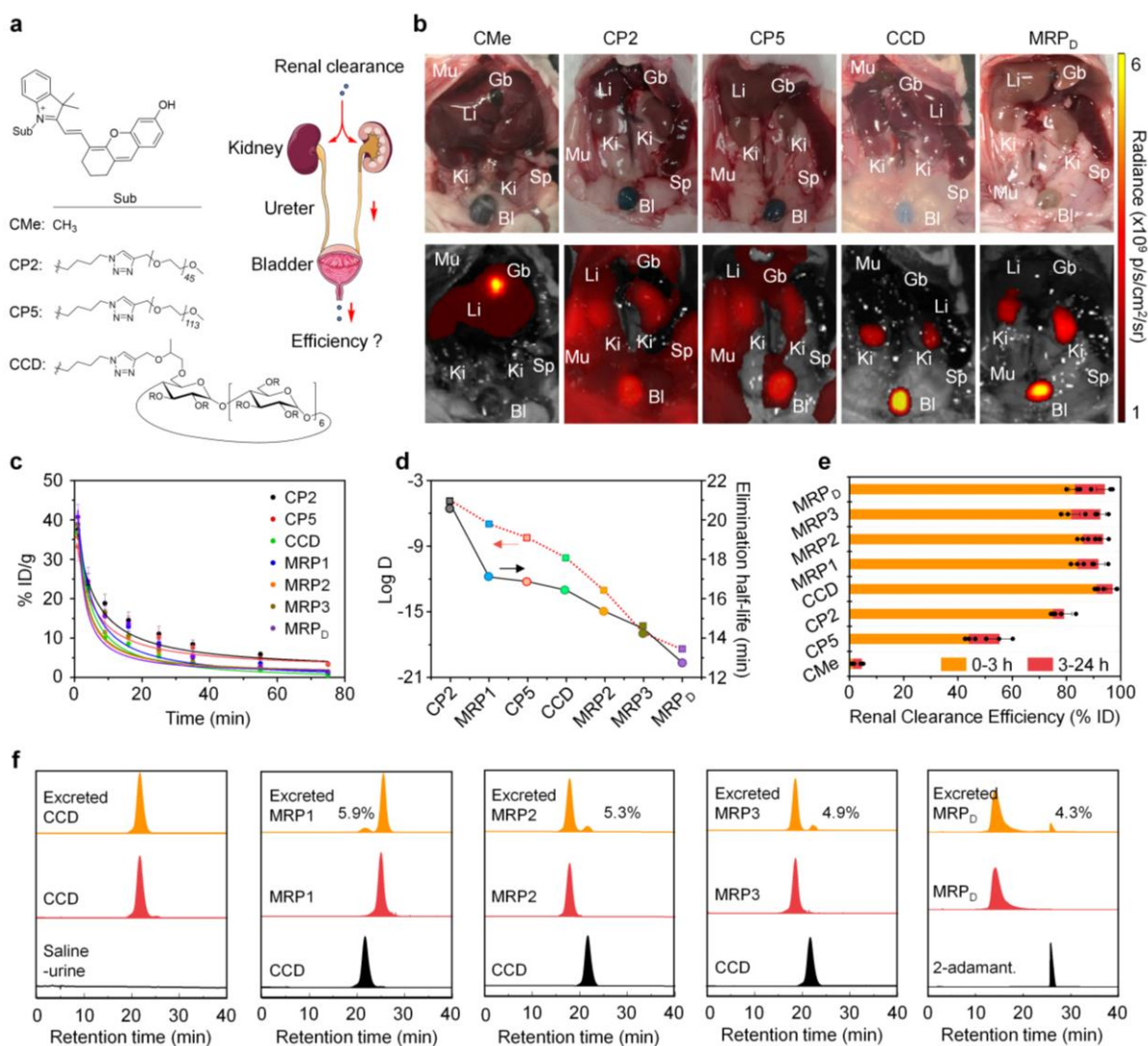
Fig. 3. Renal clearance and *in vivo* stability studies of MRPs and the uncaged fluorophores. (**a**) Chemical structures of CMe, CP2, CP5 and CCD (R = H or $CH_2CHOHCH_3$) and schematic illustration of the excretion of renal-clearable probes through the urinary tract. (**b**) NIRF images of the abdominal cavity of mice at t = 60 min after i.v. injection of CMe, CP2, CP5, CCD or MRP_D. Bladder (Bl), gallbladder (Gb), kidneys (Ki), liver (Li), muscle (Mu), spleen (Sp). NIRF images acquired at 720 nm (760 nm for MRP_D) upon excitation at 675 nm (640 nm for MRP_D) with the IVIS spectrum imaging system. (**c**) Blood concentration (%ID g^{-1}) decay of the uncaged fluorophores (CP2, CP5 and CCD) and MRPs after intravenous injection into living mice. Data are the mean ± SD. n = 3 independent mice (**d**) Correlation between elimination half-life and distribution coefficient (Log D) for the uncaged fluorophores (CP2, CP5 and CCD) and MRPs. (**e**) Renal clearance efficiency of the uncaged fluorophores (CMe, CP2, CP5, and CCD) and MRPs at 0-3 h and 3-24 h after intravenous injection. Data are the mean ± SD. n = 3 independent mice. (**f**) *In vivo* stability studies of CCD and MRPs through HPLC analysis of excreted components in the urine samples after intravenous injection. HPLC traces of the pure

compounds (CCD, MRPs and 2-adamantanone) are also indicated for comparison. The experiments in (b) and (f) were repeated independently three times with similar results.
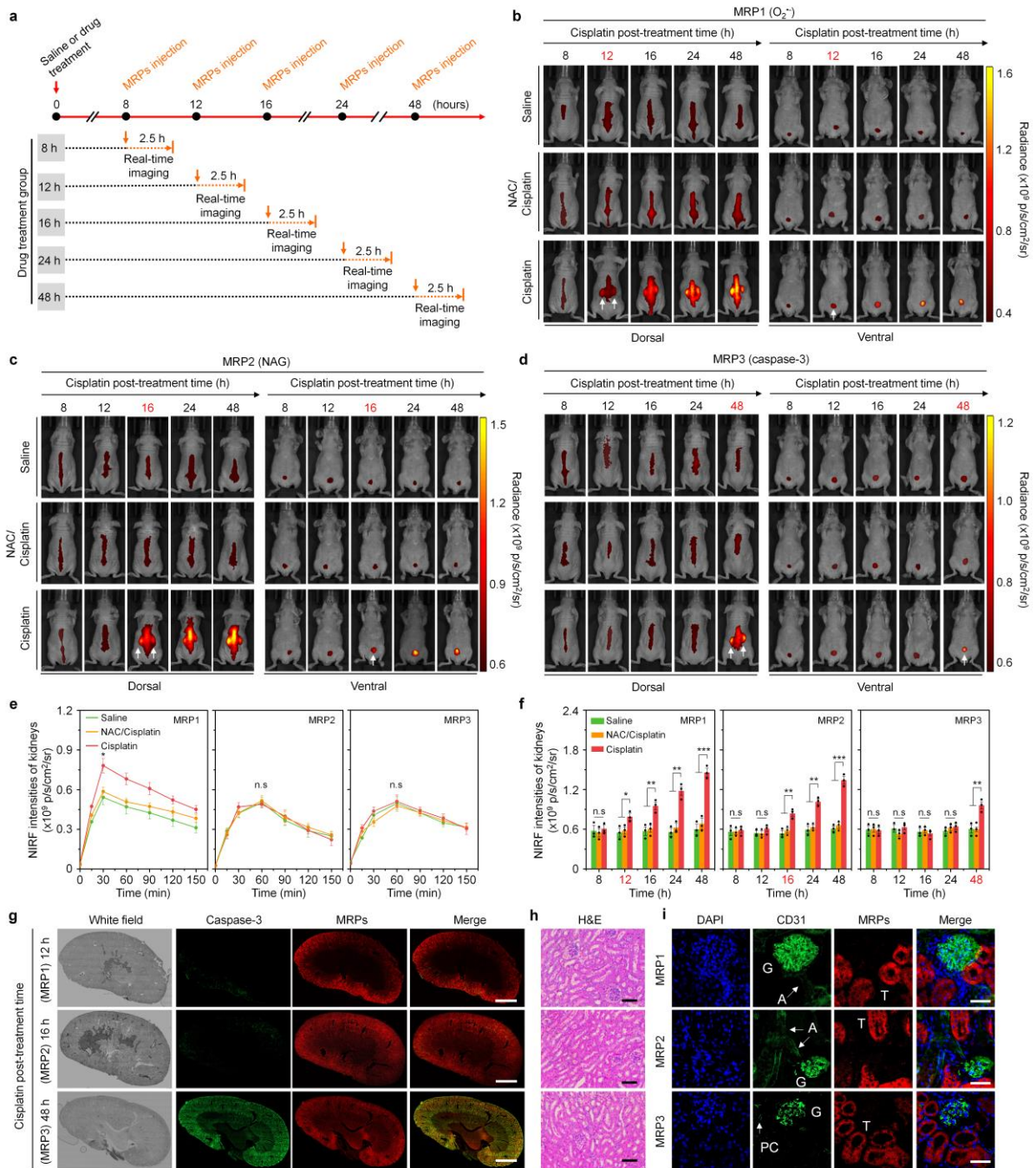
Fig. 4. Real-time *in vivo* NIRF imaging of cisplatin-induced AKI. (**a**) Schematic illustration of development of cisplatin (20 mg kg⁻¹ body weight)-induced AKI mouse model and NIRF imaging at different post-treatment timepoints. Representative NIRF images of living mice after i.v injection of MRP1 (**b**), or MRP2 (**c**), or MRP3 (**d**) at different post-treatment timepoints (8, 12, 16, 24 or 48 h). The white arrows indicate the kidneys and bladder in dorsal and ventral side, respectively. (**e**) The dynamic NIRF intensities of kidneys as a function of time post-injection of MRPs1-3 in living mice after treatment of cisplatin for 12 h. Data are the mean ± SD. n = 3 independent mice. Two-tailed student's t-test. Saline, NAC/cisplatin versus cisplatin-treated groups, n.s: not significant, *p<0.05. (**f**) NIRF intensities of kidneys in living mice *t* = 30 min after

i.v injection of MRP1 or 60 min after i.v injection of MRPs2-3 at the different post-treatment timepoints (8, 12, 16, 24 or 48 h). Data are the mean ± SD. n = 3 independent mice. Two-tailed student's t-test. Saline, NAC/cisplatin versus cisplatin-treated groups, n.s: not significant, *p<0.05, **p<0.01, ***p<0.001. (**g**) Representative confocal fluorescence microscopy images of the whole kidney slices from mice with i.v injection of MRP1, MRP2, and MRP3 at t = 12, 16 and 48 h post-treatment of cisplatin, respectively. Scale bars, 2 mm. (**h**) Representative photomicrographs of H&E staining in paraffin-embedded kidney sections from mice 12, 16, or 48 h after cisplatin treatment. Scale bar, 50 μm. (**i**) Representative confocal fluorescence microscopy images of regional kidney slices from mice with i.v injection of MRP1, MRP2, and MRP3 at t = 12, 16, and 48 h post-treatment of cisplatin, respectively. Glomerulus (G), tubules (T), arteriole (A), peritubular capillaries (PC). Scale bars, 40 μm. The experiments in (b-d) and (g-i) were repeated independently three times with similar results.
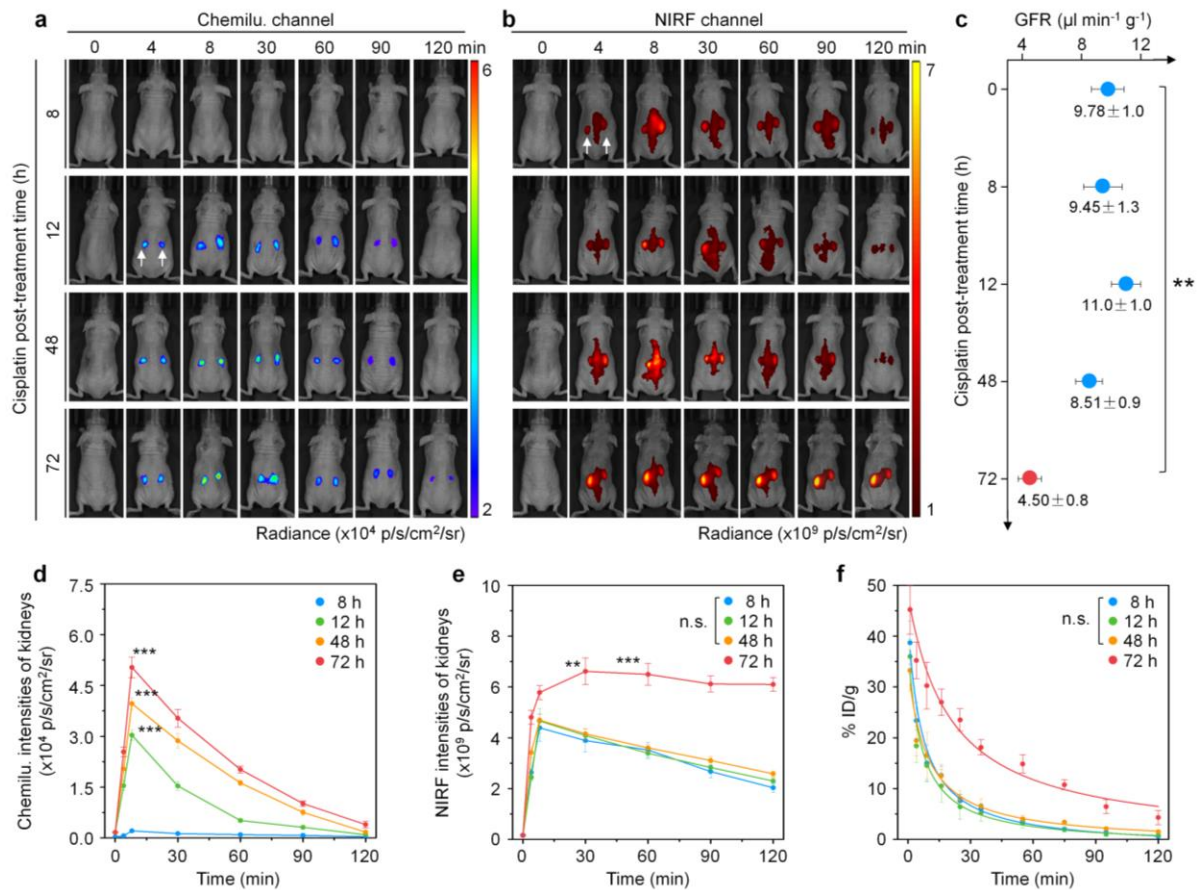

Fig. 5. Real-time *in vivo* dual-channel imaging of cisplatin-induced AKI. Representative chemiluminescence (**a**) and NIRF (**b**) images of living mice with i.v injection of MRP$_D$ after treatment of cisplatin (20 mg kg^{-1} body weight) for 8, 12, 48 or 72 h. The experiments were repeated independently three times with similar results. (**c**) GFR of living mice at t = 8, 12, 48, or 72 h post-treatment of cisplatin, or saline, measured by the standard FITC-Inulin method. Data

are the mean ± SD. n = 3 independent mice. Two-tailed student's t-test. Pre-treatment versus 8, 12, 48 h post-treatment groups, not significant; Pre-treatment versus 72 h post-treatment group, **$p<0.01$. The dynamic chemiluminescence (**d**) and NIRF (**e**) intensities of kidneys as a function of time post-injection of MRP_D in living mice after treatment of cisplatin for 8, 12, 48 or 72 h. Data are the mean ± SD. n = 3 independent mice. Two-tailed student's t-test. 8 h post-treatment versus 12, 48, or 72 h post-treatment groups, n.s: not significant, **$p<0.01$, ***$p<0.001$. (**f**) Blood concentration ($\%ID\ g^{-1}$) decay of MRP_D in the living mice at t = 8, 12, 48 or 72 h post-treatment of cisplatin. Data are the mean ± SD. n = 3 independent mice. Two-tailed student's t-test. 8 h post-treatment versus 12, or 48 h post-treatment groups, n.s: not significant.
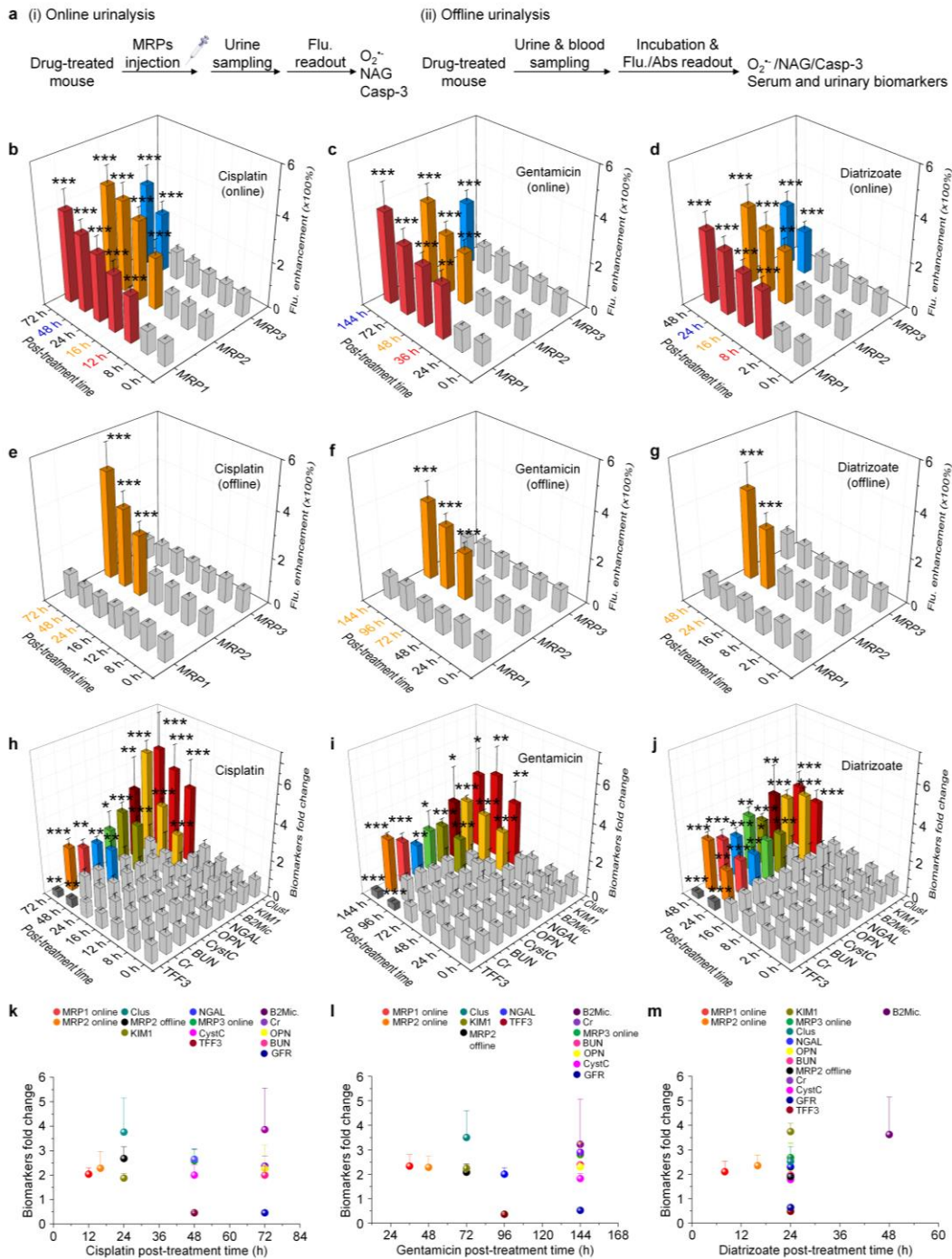
Fig. 6. In vitro diagnosis of drug-induced AKI in living mice. (**a**) Schematic illustration of the workflows for optical urinalysis of drug-induced AKI in living mice. (i) Online urinalysis: fluorescence readouts of excreted MRPs1-3 in the urine from drug-treated living mice after i.v injection of MRPs1-3 at different timepoints post-treatment of drug. (ii) Offline urinalysis: fluorescence readouts of MRPs1-3 after incubation with urine samples collected from drug-treated living mice at different timepoints post-treatment of drug. The commercial assays were used to measure Cr, BUN, and Cystatin C in the blood as well as NGAL, TFF3, OPN, β2-microglobulinin, KIM-1 and clusterin in the urine samples collected from drug-treated living mice at different timepoints post-treatment of drug. (**b-d**) Fluorescence enhancement of excreted

MRPs1-3 in the urine from drug-treated living mice after i.v injection of MRPs1-3 at different timepoints post-treatment of drug. (**e-g**) Fluorescence enhancement of MRPs1-3 after incubation with the urine samples collected from drug-treated living mice at different timepoints post-treatment of drug. Data are the mean ± SD. n = 9 independent experiments for (b-d) and (e-g). Two-tailed student's t-test. Pre-treatment versus post-treatment groups, *p<0.05, **p<0.01, ***p<0.001. (**h-j**) Fold change in urinary and serum biomarkers at different timepoints post-treatment of drug. Data are the mean ± SD. n = 5 independent experiments for Cr, BUN, Cyst C, NGAL and KIM-1, n = 6 independent experiments for TFF3, OPN, β2-Microglobulin and clusterin. Two-tailed student's t-test. Pre-treatment versus post-treatment groups, *p<0.05, **p<0.01, ***p<0.001. (**k-m**) Timeline comparing MRPs (online and offline urinalysis) to the clinical methods and FDA qualified urinary biomarkers for detection of drug-induced AKI. Data are the mean ± SD. n = 5 independent experiments for Cr, BUN, Cyst C, NGAL and KIM-1, n = 6 independent experiments for TFF3, OPN, β2-Microglobulin and clusterin.

Methods

Chemicals. All chemicals were purchased from Sigma-Aldrich or Tokyo Chemical Industry (TCI) unless otherwise stated. Cisplatin, gentamicin, diatrizoate, alpha-naphthyl isothiocyanate (ANIT) and lipopolysaccharides (LPS, from Escherichia coli 0111:B4) were obtained from Sigma-Aldrich. N-acetyl-β-D-glucosaminidase, plasmin, β-galactosidase, nitroreductase and fibroblast activation protein-alpha were purchased from Sigma-Aldrich. Alanine aminopeptidase, furin and recombinant human caspase-3 were purchased from R&D Systems. Creatinine assay kit, urea assay kit and mouse cystatin C ELISA kit were purchased from Sigma-Aldrich, BioAssay Systems and RayBiotech, respectively. Mouse NGAL, osteopontin, KIM-1, TFF3 and clusterin ELISA kit were purchased from R&D Systems. Cleaved-caspase-3 antibody (9661L) was purchased from Cell Signaling Technology. Mouse beta2-microglobulin ELISA kit, anti-CD31 antibody (ab28364), anti-CD11b antibody (ab133357) and Alexa Fluor 488 conjugated goat anti-rabbit IgG H&L (ab150077) were purchased from Abcam. Ultrapure water was supplied by Milli-Q Plus System (Millipore Corporation, Breford, USA).

Materials characterization. Silica gel (Silicycle, 230-400 mesh) was used for column chromatography. Thin layer chromatography (TLC) was carried out on silica gel glass plates coated with fluorescent indicator F-254(Merck, Germany). UV-Vis spectra were recorded on a UV-2450 spectrophotometer (Shimadzu Corporation, Japan) using quartz cuvettes. Fluorescence spectra were acquired on Fluorolog 3-TCSPC spectrofluorometer (Horiba Jobin Yvon) using quartz cuvettes. Chemiluminescence was recorded on spectramax i3x (Molecular Devices, USA) or Luminometer (Promega, USA). HPLC analyses and purification were performed on an Agilent 1260 system using acetonitrile/water as the eluent (Supplementary **Table 7**). Proton-nuclear magnetic resonance (^{1}H NMR) spectra were conducted with a Bruker 300 MHz NMR instrument. Chemical shifts are reported in ppm relative to residual protic solvent resonances. NMR spectra were analyzed by using Mestre Nova LITE v5.2.5-4119 software (Mestre lab Research S.L.). Multiplicities are reported as follows: s (singlet), d (doublet), t (triplet) or m (multiplet). Coupling constants are reported as a J value in hertz (Hz). The number of protons (n) for a given resonance is indicated nH, and based on the spectral integration values. Electrospray ionization-mass spectrometry (ESI-MS) spectra were conducted with a Thermo Finnigan Polaris Q quadrupole ion trap mass spectrometer (ThermoFisher Corporation) equipped with a standard ESI source. Matrix-assisted laser desorption/ionization time-of-flight (MALDI-TOF) analyses were conducted on a Bruker ultraflex TOF/TOF instrument. The pH values were tested by a digital pH-meter (SevenCompact S220, Zurich, Switzerland). Tissues were cut into sections using a cryostat (Leica, Germany). The tissue sections were examined using a Nikon ECLIPSE 80i

24

microscope (Nikon Instruments Inc, USA). Fluorescence microscopy images of tissue sections were acquired on a LSM800 confocal laser scanning microscope (Carl Zeiss, Germany). Fluorescence and chemiluminescence imaging were performed on the IVIS spectrum imaging system (PerkinElmer, Inc, USA). Fluorescence and chemiluminescence images were analyzed by the region of interest (ROI) analysis using the Living Image 4.3 Software. *In silico* calculation of the partition coefficients (Log D) was calculated using Marvin and JChem calculator plug-ins (ChemAxon, Hungary). Blood samples were collected using heparinized capillary tubes (Paul Marienfeld, Germany). Urine samples were collected with metabolic cages (Lab Products Inc, USA).

Synthesis of BrGlcNAc. To a solution of AcGlcNAc (0.78 g, 2.0 mmol) in anhydrous dichloromethane (8 ml) was added hydrogen bromide (33 % in acetic acid, 5 ml). The reaction mixture was stirred at 0°C for 8 h. After that, it was poured into distilled water (30 ml) under ice bath and extracted by dichloromethane (60 ml). The organic layer was washed with saturated sodium hydrogen carbonate aqueous solution (50 ml), dried over anhydrous sodium sulphate and concentrated under vacuum to afford compound BrGlcNAc (0.62 g, 75%) as a white crystalline solid. TLC (silica gel, ethyl acetate/petroleum ether, 1/3), R_f = 0.4. ^{1}H NMR (300 MHz, CDCl$_3$): δ 2.00 (s, 3H), 2.07 (s, 6H), 2.11 (s, 3H), 4.11 (d, J = 3, 1H), 4.16 (t, 1H), 4.24 (t, 1H), 5.30 (m, 2H), 5.82 (d, J = 9, 1H), 6.52 (d, J = 6, 1H). ESI-MS (m/z): calcd: 409.04, found [M-Br]: 330.1.

Synthesis of Br-Ph-DVED. Ac-DEVD (0.69 g, 1.0 mmol) was dissolved in tetrahydrofuran (20 ml), followed by addition of (4-aminophenyl) methanol (0.49 g, 4.0 mmol) and N-ethoxycarbonyl-2-ethoxy-1, 2-dihydroquinoline (0.99 g, 4.0 mmol). The reaction mixture was stirred at 25 °C for 12 h before it was concentrated under vacuum. The residue was washed with distilled water and extracted with dichloromethane. The residue was purified by HPLC to give compound Ph-DVED (0.63 g, 80%). Ph-DVED (0.40 g, 0.5 mmol) was dissolved in tetrahydrofuran (25 ml), followed by addition of phosphorus tribromide (0.27 g, 1.0 mmol). The reaction mixture was stirred at 25 °C for 12 h and then quenched with distilled water, followed by extraction with dichloromethane and concentrated under vacuum. The residue was purified by HPLC to afford compound Br-Ph-DVED (0.32 g, 76% yield). ^{1}H NMR (300 MHz, CDCl$_3$): δ 0.95 (s, 6H), 1.43 (s, 27H), 2.08 (s, 3H), 2.22 (m, 3H), 2.53 (m, 3H), 2.85 (m, 4H), 4.35 (m, 3H), 4.76 (s, 3H), 7.11 (d, J = 6 Hz, 1H), 7.31 (d, J = 3 Hz, 1H), 7.52 (d, J = 3 Hz, 1H), 7.92 (s, 1H). ESI-MS (m/z): calcd: 853.35, found [M-Br]: 774.21.

Synthesis of propynyl-HPβCD. To a solution of HPβCD (3.08 g, 2.0 mmol) and tetra-tert-butylammonium iodide (0.16 g, 0.44 mmol) in anhydrous dimethylformamide (15 ml) was added a suspension of sodium hydride (0.80 g, 20 mmol, 60% dispersion in mineral oil) in anhydrous dimethylformamide (25 ml) at 0 °C. After stirring for 0.5 h at 0 °C, a solution of

propargyl bromide (0.30 g, 3.0 mmol) in anhydrous dimethylformamide (1 ml) was added. The reaction mixture was stirred at 25 °C for additional 24 h before it was concentrated under vacuum. The residue was purified by silica gel column chromatography (methanol/ethylacetate = 1/2 and methanol/H_2O = 4/1) to afford propynyl-HPβCD (3.02 g, 94%) as a yellowish solid after freeze dry. ^{1}H NMR (300 MHz, D_2O): δ 1.14 (d, J = 6, 17H), 2.72 (s, 1H), 3.25-4.25 (m, 64H), 5.08-5.25 (m, 7H). MALDI-TOF MS found: 1400-1800.

Synthesis of CMe and CyOH. CMe and CyOH were synthesized according to our previous study[28]. ^{1}H NMR of CMe (300 MHz, CDCl$_3$): δ 1.65 (s, 6H), 1.88 (m, 2H), 2.63 (m, 4H), 3.33 (s, 3H), 5.54 (d, J = 15 Hz, 1H), 6.55 (s, 1H), 6.76 (m, 2H), 7.04-7.24 (m, 3H), 7.29 (m, 2H), 8.03 (t, 1H). ESI-MS of CMe (m/z): calcd: 384.19, found: 384.40. ^{1}H NMR of CyOH (300 MHz, CDCl$_3$): δ 1.76 (s, 6H), 1.96 (m, 8H), 2.71 (t, 2H), 3.47 (t, 2H), 4.21 (d, J = 6 Hz, 2H), 5.30 (s, 1H), 6.11 (d, J = 15 Hz, 1H), 7.17 (m, 3H), 7.44 (m, 4H), 7.71 (m, 1H), 8.50 (d, J = 15 Hz, 1H). ESI-MS of CyOH (m/z): calcd: 467.2, found: 467.2.

Synthesis of MRP1. A mixture of CyOH (46.70 mg, 0.1 mmol), diphenylphosphinyl chloride (46.0 μl, 0.24 mmol) and triethylamine (56.0 μl, 0.4 mmol) in dichloromethane (10 ml) was stirred at 25 °C. After 15 min, the reaction mixture was concentrated under vacuum to afford compound CS as a blue solid, which was used in the next step without further purification. ESI-MS (m/z): calcd: 667.2, found: 667.3. Compound CS (83 mg, 0.125 mmol) was dissolved in distilled water (1 ml) and stirred at 25 °C for 10 min. To above solution, propynyl-HPβCD (0.20 g, 0.125 mmol), sodium ascorbate (4.60 mg, 0.022 mmol) and cupric sulfate (7.50 mg, 0.03 mmol) in DMSO/water (2 ml/2 ml) was added. The mixture was stirred at 25 °C under a nitrogen atmosphere in dark for 5 h, and then precipitated in acetone (350 ml). The crude product was filtered and further purified by HPLC to afford MRP1 (0.20 g, 80% yield) as a blue solid. ^{1}H NMR (300 MHz, D_2O): δ 1.14 (m, 18H), 1.73-2.12 (m, 15H), 2.45 (m, 2H), 2.94 (m, 3H), 3.25-4.25 (m, 83H), 4.28 (m, 2H), 5.07-5.31 (m, 13H), 5.58 (m, 2H), 6.04 (s, 1H), 6.85-8.47 (m, 16H). MALDI-TOF MS found: 1600-2300.

Synthesis of MRP2. A mixture of compound CyOH (23.40 mg, 0.05 mmol) and cesium carbonate (0.07 g, 0.2 mmol) in anhydrous dichloromethane (3 ml) was stirred at 25 °C under a nitrogen atmosphere for 15 min. To above solution, BrGlcNAc (0.08 g, 0.2 mmol) was added and stirred at 25 °C for additional 16 h. Then the reaction was poured into distilled water (15 ml), extracted by dichloromethane (60 ml) and concentrated under vacuum to yield crude product. To a solution of above crude product (26.40 mg, 0.033 mmol) in methanol (4 ml), sodium methoxide solution (0.07 g, 0.33 mmol, 25% in methanol) was added. The reaction mixture was stirred at 25 °C for 10 min and then evaporated under vacuum. The crude product was purified by silica gel column chromatography (dichloromethane/methanol = 8/1) for afford compound CN as a blue solid. ^{1}H NMR (300

MHz, CD$_3$OD): δ 1.84 (d, 3H), 1.91 (s, 6H), 2.00 (m, 4H), 2.03 (s, 2H), 2.18 (m, 2H), 2.76 (m, 2H), 3.45 (m, 2H), 3.60-4.10 (m, 6H), 4.41 (s, 2H), 4.61 (d, J = 9 Hz, 1H), 5.11 (d, J = 3 Hz, 1H), 5.34 (t, 1H), 6.56 (d, J = 15 Hz, 1H), 7.03 (d, J = 3 Hz, 1H), 7.20 (s, 1H), 7.40-7.60 (m, 5H), 8.79 (d, J = 15 Hz, 1H). ESI-MS (m/z): calcd: 670.3, found: 670.3. Compound CN (23 mg, 0.033 mmol) and propynyl-HPβCD (53 mg, 0.033 mmol) were dissolved in DMSO/water (2 ml/2 ml), followed by addition of a solution of sodium ascorbate (2.0 mg, 0.01 mmol) and cupric sulfate (2.5 mg, 0.01 mmol) in distilled water. After the reaction mixture was stirred at 25 °C under a nitrogen atmosphere in dark for 5 h, it was precipitated in acetone (350 ml). The crude product was filtered and further purified by HPLC to afford MRP2 (58 mg, 85% yield) as a blue solid. ^{1}H NMR (300 MHz, D$_2$O): δ 1.20 (m, 18H), 1.80-2.13 (m, 15H), 2.70 (m, 3H), 3.00 (m, 3H), 3.25-4.25 (m, 70H), 4.32 (m, 3H), 5.15-5.31 (m, 9H), 5.60-5.75 (m, 2H), 6.57 (d, J = 15, 1H), 7.04-7.72 (m, 7H), 8.80 (d, J = 15, 1H). MALDI-TOF MS found: 1600-2300.

Synthesis of MRP3. To a solution of compound CyOH (23.40 mg, 0.05 mmol) in acetonitrile (10 ml) were added compound Br-Ph-DVED (0.13 g, 0.15 mmol) and N,N-diisopropylethylamine (79 µL, 0.62 mmol). After the reaction mixture was stirred at 70 °C for 4 h, it was poured into distilled water (15 ml) and extracted by dichloromethane and concentrated under vacuum to yield crude product. Trifluoroacetic acid (1 ml) and dichloromethane (2 ml) were added to the residue, and the reaction mixture was stirred for additional 30 min at 25 °C before being concentrated under vacuum. The residue was purified by HPLC to give compound CC as a blue solid (49 mg, 91%). ^{1}H NMR (300 MHz, CD$_3$OD): δ 1.22 (s, 12H), 1.53 (m, 2H), 1.76 (m, 4H), 1.92 (t, 6H), 2.10 (t, 2H), 2.35 (t, 2H), 2.66 (m, 5H), 3.00 (m, 2H), 3.36 (m, 2H), 3.95 (t, 1H), 4.26 (t, 2H), 4.58 (t, 1H), 5.19 (m, 3H), 6.42 (d, J = 15 Hz, 2H), 6.97 (s, 2H), 7.35 (m, 4H), 7.63 (m, 4H), 8.67 (d, J = 15 Hz, 2H). ESI-MS (m/z): calcd: 1072.48, found: 1072.47. Compound CC (22 mg, 0.02 mmol) and propynyl-HPβCD (32 mg, 0.02 mmol) was dissolved in DMSO/water (2 ml/2 ml). A solution of sodium ascorbate (4.10 mg, 0.02 mmol) and cupric sulfate (8.30 mg, 0.033 mmol) in distilled water was added. After the mixture was stirred at 25 °C under a nitrogen atmosphere in dark for 5 h, it was precipitated in acetone (350 ml). The crude product was filtered and further purified by HPLC to afford MRP3 (45 mg, 84% yield) as a blue solid. ^{1}H NMR (300 MHz, D$_2$O): δ 1.21 (m, 16H), 1.48-1.74 (m, 8H), 2.12-2.32 (m, 6H), 2.38 (s, 2H), 3.02 (m, 3H), 3.25-4.25 (m, 51H), 4.32-4.55 (m, 5H), 5.15-5.32 (m, 9H), 6.17 (d, J = 12, 1H), 6.40 (d, J = 9, 1H), 7.03-8.66 (m, 12H). MALDI-TOF MS found: 2350-2850.

Synthesis of CP2 and CP5. To a mixture of CyOH (9.40 mg, 0.02 mmol) and methoxy-PEG-alkyne (MW: 2000 or 5000, 1.5 equiv to CyOH) in DMSO/water (2 ml/2 ml) was added a solution of sodium ascorbate (1.05 mg, 0.005 mmol) and cupric sulfate (1.06 mg, 0.004

mmol) in distilled water. After the mixture was stirred at 25 °C under a nitrogen atmosphere in dark for 5 h, it was precipitated in acetone (350 ml). The crude product was filtered and further purified by HPLC to afford CP2 (41 mg, 81% yield) and CP5 (92 mg, 83%) as a blue solid. ^{1}H NMR of CP2 (300 MHz, D$_2$O): δ 1.60-1.82 (m, 8H), 1.83 (m, 2H), 2.48 (m, 4H), 3.37 (m, 2H), 3.4-4.0 (m, 177H), 4.54 (t, 4H), 6.00-8.21 (m, 10H). ^{1}H NMR of CP5 (300 MHz, D$_2$O): δ 1.51 (m, 6H), 1.83 (m, 4H), 2.43 (s, 4H), 3.25-4.25 (m, 200H), 4.16-4.30 (m, 4H), 5.63-7.94 (m, 10H). MALDI-TOF MS found: 1400-3000 and 4000-7000 for CP2 and CP5, respectively.

Synthesis of CCD. CyOH (46.70 mg, 0.1 mmol), propynyl-HPβCD (0.20 g, 0.125 mmol), sodium ascorbate (4.60 mg, 0.022 mmol) and cupric sulfate (7.50 mg, 0.03 mmol) was dissolved in DMSO/water (2 ml/2 ml) and stirred at 25 °C under a nitrogen atmosphere in dark for 5 h. Then the reaction was precipitated in acetone (350 ml). The crude product was filtered and further purified by HPLC to afford CCD (0.22 g, 86%) as a blue solid. ^{1}H NMR (300 MHz, D$_2$O): δ 1.23 (s, 18H), 1.85 (s, 6H), 1.99 (m, 6H), 2.72 (m, 2H), 3.05 (t, 2H), 3.25-4.25 (m, 74H), 4.34 (t, 1H), 4.57 (t, 2H), 5.18 (m, 9H), 5.62 (t, 2H), 6.59-7.72 (m, 10H). MALDI-TOF MS found: 1600-2180.

Synthesis of compound 5. A mixture of 3-hydroxybenzaldehyde (compound 4, 2.44 g, 20 mmol), trimethyl orthoformate (3.58 ml, 32 mmol), and tertrabutylammonium tribromide (0.49 g, 1.0 mmol) in methanol (30 ml) was stirred at 25 °C under a nitrogen atmosphere for 16 h. The reaction mixture was concentrated under vacuum to remove methanol, then poured into saturated sodium bicarbonate aqueous solution (200 ml), extracted with ethyl acetate (200 ml), and concentrated under vacuum. The residue was purified by silica gel column chromatography to afforded compound 5 (3.20 g, 95% yield) as colorless oil. TLC (silica gel, ethyl acetate/petroleum ether = 1/5), R$_f$ = 0.42. ^{1}H NMR (300 MHz, CDCl$_3$): δ 3.37 (s, 6H), 5.39 (s, 1H), 6.17 (s, 1H), 6.83 (m, 1H), 7.02 (m, 2H). ESI-MS (m/z): calcd: 168.08, found [M-Br]: 168.21.

Synthesis of compound 6. A mixture of 3-hydroxybenzaldehyde dimethyl acetal (compound 5, 2.52 g, 15.0 mmol), imidazole (1.53 g, 22.5 mmol) and tert-butyldimethylsilyl chloride (2.70 g, 18.0 mmol) in dichloromethane (20 ml) was stirred at 25 °C. After 16 h, the white precipitate was filtered off and the solvent was evaporated under reduced pressure. The residue was purified by silica gel column chromatography to afforded compound 6 (3.85 g, 91% yield) as colorless oil. TLC (silica gel, ethyl acetate/ petroleum ether = 1/15), R$_f$ = 0.45. ^{1}H NMR (300 MHz, CDCl$_3$): δ 0.23 (s, 6H), 1.02 (s, 9H), 3.36 (s, 6H), 5.38 (s, 1H), 6.82 (d, J = 3 Hz, 1H), 6.97 (s, 1H), 7.06 (d, J = 9 Hz, 1H), 7.30 (m, 1H). ESI-MS (m/z): calcd: 282.17, found: 282.30.

Synthesis of compound 7. Acetal (compound 6, 3.38 g, 12.0 mmol) and trimethyl phosphite (2.13 ml, 18.0 mmol) was dissolved in dichloromethane (40 ml) and stirred in ice bath. Titanium (IV) chloride (2.38 ml, 18.0 mmol) was dropwise added and stirred for 16 h. The solution was poured into a saturated sodium bicarbonate aqueous solution (200 ml) in ice bath. After stirring for 15 min, the mixture was extracted by dichloromethane (200 ml) and concentrated under vacuum to yield crude product as colorless oil. The residue was purified by silica gel column chromatography to afforded compound 7 (3.24 g, 75% yield) as colorless oil. TLC (silica gel, ethyl acetate/petroleum ether = 2/1), R_f = 0.52. ^{1}H NMR (300 MHz, CDCl$_3$): δ 0.21 (s, 6H), 0.99 (s, 9H), 3.38 (s, 3H), 3.69 (t, 6H), 4.48 (d, J = 15 Hz, 1H), 6.81 (d, J = 9 Hz, 1H), 6.94 (s, 1H), 7.01 (d, J = 6 Hz, 1H), 7.24 (m, 1H). ESI-MS (m/z): calcd: 360.15, found: 360.81.

Synthesis of compound 8. Phosphonate (compound 7, 3.24 g, 9.0 mmol) was dissolved in anhydrous THF (20 ml) under a nitrogen atmosphere at -78 °C. To above solution, lithium di-isopropyl amide (2.0 M in THF, 6 ml, 10.35 mmol) was added and the solution was stirred for 0.5 h. 2-adamantanone (1.62 g, 10.8 mmol) in anhydrous THF (20 ml) was added and stirred for 0.5 h min at -78 °C, then stirred at 25 °C for additional 3 h. The reaction mixture was poured into brine (200 ml), extracted with ethyl acetate (200 ml) and concentrated under vacuum. The residue was purified by silica gel column chromatography to give compound 8 (2.94 g, 85% yield) as colorless oil. TLC (silica gel, ethyl acetate/ petroleum ethe = 1/15), R_f = 0.65. ^{1}H NMR (300 MHz, CDCl$_3$): δ 0.20 (s, 6H), 0.98 (s, 9H), 1.78-1.97 (m, 13H), 3.25 (s, 1H), 3.38 (s, 3H), 6.75 (m, 2H), 6.79 (d, J = 3 Hz, 1H), 7.20 (t, 1H). ESI-MS (m/z): calcd: 384.25, found [M-Br]: 384.40.

Synthesis of compound 9. compound 8 (2.94 g, 6.8 mmol) and tetrabutylammonium fluoride (1.0 M in THF, 7.5 ml, 7.5 mmol) was dissolved in anhydrous THF (30 ml) and stirred for 12 h at 25 °C . The reaction mixture was poured into hydrogen chloride aqueous solution (1M, 100 ml), extracted with ethyl acetate (200 ml) and concentrated under vacuum. The residue was purified by silica gel column chromatography to afforded compound 9 (1.74 g, 95% yield) as a white solid. TLC (silica gel, ethyl acetate/ petroleum ether = 1/15), R_f = 0.30. ^{1}H NMR (300 MHz, CDCl$_3$): δ 1.79-1.97 (m, 12H), 2.65 (s, 1H), 3.25 (s, 1H), 3.33 (s, 3H), 5.58 (s, 1H), 6.80 (m, 1H), 6.86 (t, 2H), 7.22 (t, 1H). ESI-MS (m/z): calcd: 270.16, found: 270.18.

Synthesis of compound 10. To a solution of compound 9 (1.70 g, 6.3 mmol) in toluene (150 ml) was added N-Iodosuccinimide (NIS, 1.42 g, 6.3 mmol) in ice bath and stirred at 25 °C for 12 h. The reaction mixture was poured into saturated sodium thiosulfate aqueous solution, extracted with ethyl acetate (200 ml) and concentrated under vacuum. The residue was purified by silica gel column chromatographyto afford compound 10 (1.97 g, 80% yield)

as a white solid. TLC (silica gel, ethyl acetate/petroleum ether = 1/5), R_f = 0.70. ^{1}H NMR (300 MHz, CDCl$_3$): δ 1.77-1.95 (m, 12H), 2.62 (s, 1H), 3.22 (s, 1H), 3.29 (s, 3H), 5.27(s, 1H), 6.63 (d, J = 3, 1H), 6.94 (s, 1H), 7.59 (d, J = 9, 1H). ESI-MS (m/z): calcd: 396.06, found [M-I]: 269.10.

Synthesis of CL. To a mixture of iodophenol (compound 9, 1.78 g, 4.5 mmol), methyl acrylate (1.16 g, 13.5 mmol) and triethylamine (0.68 g, 6.75 mmol) in anhydrous acetonitrile (30 ml) was added palladium(II) acetate (Pd(OAc)$_2$, 50.50 mg, 0.225 mmol) and tri(o-tolyl)phosphine (P(o-tol)$_3$,13.70 mg, 0.045 mmol). The flask was sealed and the reaction was stirred at 90 °C for 12 h. Then the reaction mixture was poured into saturated ammonium chloride aqueous solution (200 ml), extracted with ethyl acetate (200 ml), and concentrated under vacuum. The residue was purified by silica gel column chromatography to give compound CL (1.27 g, 80% yield) as a pale-yellow solid. TLC (silica gel, ethyl acetate/petroleum ether = 1/1), R_f = 0.50. ^{1}H NMR (300 MHz, CDCl$_3$): δ 1.79-1.96 (m, 12H), 2.69 (s, 1H), 3.23 (s, 1H), 3.33 (s, 3H), 3.81 (s, 3H), 6.38 (s, 1H), 6.58 (d, J = 18 Hz, 1H), 6.86 (s, 2H), 7.41 (d, 1H), 7.95 (d, J = 18 Hz, 1H). ESI-MS (m/z): calcd [(M+H)$^+$]: 355.18, found: 355.15.

Synthesis of compound 11. Compound CL (1.27 g, 3.6 mmol) and anhydrous pyridine (10 ml) was stirred in anhydrous dichloromethane (15 ml) at -78 °C under a nitrogen atmosphere. Trifluoromethanesulfonic anhydride (1.22 ml, 7.2 mmol) was dropwise added to the solution. The mixture was kept stirring at -78 °C for 0.5 h and then at 25 °C for additional 2 h. The reaction was quenched by saturated sodium bicarbonate aqueous solution at 25 °C, extracted by ethyl acetate (100 ml). The organic layer was washed three times with hydrogen chloride (1 M, 150 ml) concentrated under vacuum. The residue was purified by silica gel column chromatography to afford compound 11 (1.58 g, 90% yield) as a pale-yellow solid. TLC (silica gel, ethyl acetate/ petroleum ether = 1/6), R_f = 0.60. ^{1}H NMR (300 MHz, CDCl$_3$): δ 1.81-1.99 (m, 12H), 2.69 (s, 1H), 3.26 (s, 1H), 3.33 (s, 3H), 3.84 (s, 3H), 6.49 (s, J = 15 Hz, 1H), 7.32 (t, 2H), 7.66 (d, J = 9 Hz, 1H), 7.84 (d, J = 18 Hz, 1H). ESI-MS (m/z): calcd [(M+H)$^+$]: 487.13, found: 487.09.

Synthesis of compound 12. Compound 11 (1.50 g, 3.08 mmol) and sodium hydroxide (NaOH, 0.25 g, 6.16 mmol) were dissolved in THF (20 ml) and H$_2$O (5 ml). Reaction mixture was stirred at 60 °C for 4 h and monitored by TLC. Upon completion, the reaction mixture washed with hydrogen chloride (0.5 M, 100 ml), extracted with ethyl acetate (150 ml) and evaporated under vacuum. The residue was purified by silica gel column chromatography to afford compound 12 (1.38 g, 95% yield) as a pale-yellow solid. TLC (silica gel, ethyl acetate/petroleum ether = 1/1), R_f = 0.42. ^{1}H NMR (300 MHz, CD$_3$OD): δ 1.76-1.92 (m, 12H),

2.69 (s, 1H), 3.22 (s, 1H), 3.25 (s, 3H), 6.54 (d, J = 18 Hz, 1H), 7.23 (s, 1H), 7.35 (d, J = 9 Hz, 1H), 7.74 -7.86 (m, 2H). ESI-MS (m/z): calcd: 472.12, found: 472.16.

Synthesis of CSCL. Compound 12 (1.30 g, 2.75 mmol) and methylene blue (32 mg, 0.1 mmol) were dissolved in a mixture of dichloromethane and methanol (10 ml/10 ml). Oxygen was bubbled through the solution while irradiating with yellow light for 120 min. The reaction mixture was concentrated under vacuum in 30 °C water bath. The crude product was purified by preparative HPLC to afford CSCL (0.83 g, 60% yield) as a white solid. ^{1}H NMR (300 MHz, CDCl$_3$): δ 0.86 (t, 1H), 1.25 (s, 1H), 1.75-1.92 (m, 10H), 2.92 (s, 1H), 3.26 (s, 3H), 6.32 (d, J = 9 Hz, 1H), 7.19 (s, J = 6 Hz, 1H), 7.37 -7.65 (m, 3H). ESI-MS (m/z): calcd: 504.11, found [M-H]: 503.20.

Synthesis of Cy7NH2. CyCl (0.26 g, 0.4 mmol) and N-Fmoc-1, 3-diaminopropane hydrochloride (0.33 g, 1.0 mmol) were dissolved in dimethylformamide (10 ml) and stirred at 65 °C for 4 h. After cooling down, the mixture was poured into distilled water (35 ml), extracted using dichloromethane, and concentrated under vacuum to yield crude product compound 13 as a blue solid. A mixture of compound 13 and piperidine (1 ml) in dichloromethane (4 ml) was stirred at 25 °C for 60 min. The reaction was poured into distilled water (30 ml), extracted by using dichloromethane, and concentrated under vacuum. The residue was purified by silica gel column chromatography to afford compound Cy7NH2 (0.15 g, 55% yield) as a blue solid. TLC (silica gel, dichloromethane/methanol = 15/1), R$_f$ = 0.46. ^{1}H NMR (300 MHz, CDCl$_3$): δ 1.62 (m, 12H), 1.86 (m, 12H), 2.47 (t, 4H), 3.09 (t, 4H), 3.35 (m, 4H), 3.81-3.95 (m, 4H), 5.54 (d, J = 12 Hz, 2H), 6.79-6.87 (m, 4H), 7.24(m, 2H), 7.64 (m, 4H). ESI-MS (m/z): calcd: 687.46, found: 687.50.

Synthesis of CySCL. A mixture of Cy7NH2 (0.14 g, 0.2 mmol), CSCL (0.11 mg, 0.2 mmol), N,N-diisopropylethylamine (12.90 mg, 0.1 mmol) and (2-(1H-benzotriazol-1-yl)-1,1,3,3-tetramethyluronium hexafluorophosphate (0.15 g, 0.4 mmol) in dimethylformamide (6 ml) was stirred at 25 °C for 4 h. The reaction was poured into distilled water (40 ml), extracted by dichloromethane, and concentrated under vacuum. The residue was purified by silica gel column chromatography to afford compound CySCL (0.18 g, 75% yield) as a blue solid. TLC (silica gel, dichloromethane/methanol = 15/1), R$_f$ = 0.65. ^{1}H NMR (300 MHz, CDCl$_3$): δ 0.92 (m, 1H), 1.25 (s, 1H), 1.60-2.06 (m, 34H), 2.48 (m, 4H), 2.90 (t, 1H), 3.29 (s, 3H), 3.31 (m, 4H), 3.39 (m, 4H), 3.82-3.94 (m, 4H), 5.59 (d, J = 9 Hz, 2H), 6.29 (t, 1H), 6.83 (m, 3H), 7.03 (m, 3H), 7.23 (m, 2H), 7.29 (m, 2H), 7.38 (m, 3H), 7.54 (m, 1H), 7.70 (m, 1H). ESI-MS (m/z): calcd: 1173.56, found: [M-H] 1172.40.

Synthesis of MRP$_D$. A mixture of CySCL (0.18 g, 0.15 mmol), propynyl cyclodextrin (0.60 g, 0.375 mmol), sodium ascorbate (6.80 mg, 0.033 mmol) and cupric sulfate (8.30 mg, 0.033 mmol) in the solution of DMSO/water (3 ml/3 ml) was stirred in ice bath under a nitrogen

atmosphere in dark for 5 h. Then the mixture was precipitated in acetone (350 ml). The crude product was filtered and further purified by HPLC to yield a blue solid MRP_D (0.52 g, 80% yield). ^{1}H NMR (300 MHz, D_2O): δ 0.90 (m, 1H), 1.26 (s, 21H), 1.64-2.10 (m, 34H), 2.58 (m, 4H), 2.83 (t, 2H), 3.20 (m, 4H), 3.25-4.25 (m, 100H), 4.24 (t, 4H), 4.37 (t, 2H), 4.48 (t, 2H), 5.00-5.16 (m, 14H), 5.65 (t, 2H), 6.86-7.11 (m, 10H), 7.47-7.79 (m, 6H). MALDI-TOF MS found: 3400-4400.

Preparation of stock solutions. MRPs and the uncaged fluorophores (CMe, CP2, CP5 and CCD) were dissolved in PBS buffer (10 mM, pH 7.4) to obtain stock solutions. 10% DMSO/PBS buffer are co-solvents for CMe. Stock solutions of H_2O_2, HOCl, and $O_2^{\cdot-}$ were prepared by directly diluting H_2O_2, NaOCl, and KO_2, respectively. •OH was prepared by Fenton reaction between H_2O_2 and $Fe(ClO_4)_2$. [1]O_2 was generated by addition NaOCl to H_2O_2. $ONOO^-$ was generated from 3-morpholinosydnonimine hydrochloride. Stock solutions of histidine, glutathione, N-acetylcysteine, ascorbic acid, hydroquinone, caspase-3, fruin, nitroreductase, β-galactosidase, fibroblast activation protein-alpha, alanine aminopeptidase, *N*-acetyl-β-D-glucosaminidase, NaCl, KCl, $MgSO_4$, $CaCl_2$, $FeSO_4$ were prepared with distilled water.

Optical Measurement. MRP1, MRP2, MRP3 and MRP_D solutions (30 μM) were incubated with their respective biomarkers (60 μM KO_2, 40 mU NAG, 0.5 μg caspase-3 and 60 μM KO_2, respectively) in PBS (10 mM, pH 7.4) at 37 °C. UV-Vis absorption and fluorescence spectra of the solutions were measured on UV-Vis and fluorescence spectrophotometer after 60 min incubation. Fluorescence images were acquired using the IVIS spectrum imaging system with excitation at 675 ± 10 nm (640 ± 10 nm for MRP_D) and emission at 720 ± 10 nm (760 ± 10 nm for MRP_D) and the acquisition time of 0.1 s. Chemiluminescence images were acquired under bioluminescence mode with open filter and the acquisition time of 1 s. The sensing capability of MRPs was analyzed through HPLC. UV-Vis absorption and fluorescence spectra of the uncaged fluorophores solution (30 μM) in PBS (10 mM, pH 7.4) were recorded on UV-Vis and fluorescence spectrophotometers.

***In vitro* selectivity studies.** MRP1 and MRP_D (30 μM) were treated with indicated ROS (150 μM) and other analytes (150 μM) in PBS (10 mM, pH 7.4) at 37 °C for 60 min. MRP2 and MRP3 (30 μM) were incubated with indicated ROS (150 μM), metal ions (150 μM), and enzymes including caspase-3 (0.5 μg) in PBS (10 mM, 50 mM NaCl, 0.1% Chaps, 10 mM EDTA, 5% Glycerol, 1 mM DTT, pH 7.4), alanine aminopeptidase (1.0 U) in HEPES buffer (10 mM, pH 7.4), furin (40 mU) in Tris buffer (25 mM, 1 mM $CaCl_2$, 0.5% (w/v) Brij-35, pH 9.0), nitroreductase (1.0 U) in Tris buffer (10 mM, 1 mM NADH, 1 mM K_2CrO_4, pH 7.0), plasmin (1.0 U) in lysine Buffer (100 mM, pH 7.5), β-Galactosidase (1.0 U) in acetate buffer (10 mM, pH 4.5), fibroblast activation protein-alpha (0.9 U) in HEPES buffer (50 mM, 1 mg

mL^{-1} BSA, 5% glycerol, pH 7.4), or NAG (40 mU) in PBS (10 mM, pH 7.4) at 37 ºC for 60 min. Fluorescence or chemiluminescence enhancement of MRPs was measured on fluorescence spectrophotometer or spectramax after incubation. Unit definition: 1 U of enzyme will hydrolyze 1 µmol of the corresponding substrate per minute at optimized condition. PBS was purged with nitrogen gas for 35 min before used in these experiments.

Measurement of the limit of detection (LOD). Fluorescence intensities (720 nm) of MRP1 (30 µM) and chemiluminescence intensities (540 nm) of MRP$_D$ (30 µM) were measured upon addition of aliquots of micromolar concentration of KO_2. The LOD was calculated using the equation[46]: LOD = 3σ/k, where σ represents the standard deviation of emission intensities of blank, and k represents the slope of the plot of emission intensities against the concentration of KO_2.

Enzyme kinetic assay. Various concentrations of MRP2 (5, 10, 15, 20, 25, 30, 35, 40, 45, 50 or 55 µM) or MRP3 (5, 10, 15, 20, 30, 40, 50 or 60 µM) were incubated with NAG (40 mU) or caspase-3 (0.5 µg) at 37 ºC for 15 min in PBS (10 mM, pH 7.4). After incubation, the mixtures were analyzed using HPLC for quantification. The initial reaction velocity (nM s^{-1}) was calculated, plotted against the concentration of MRP2 or MRP3, and fitted to a Michaelis-Menten curve. The kinetic parameters were calculated by use of the Michaelis-Menten equation[47]: $V = V_{max}*[S]/(K_m + [S])$, where V is the initial velocity, and [S] is substrate concentration.

Measurement of fluorescence quantum yields. ICG was used as a standard with a known fluorescence quantum yield (Φ) value of 13% in DMSO[48]. Fluorescence quantum yields were calculated using the following equation: $\Phi_s/\Phi_f = (A_s/A_f) \times (Abs_s/Abs_f) \times (\eta_s^2/\eta_f^2)$, Where Φ_s and Φ_f are the fluorescence quantum yields of the standard and the samples, respectively; A_s and A_f are the emission areas of the standard and the samples, respectively; Abs_s and Abs_f are the absorbance of the standard and the samples at the wavelength of excitation; η_s and η_f are the refractive indices of the standard and the samples, respectively.

Determination of chemiluminescence kinetic profiles. MRP$_D$ solution (30 µM) in PBS (10 mM, pH 7.4) was placed in a black 96-well plate. Chemiluminescence intensities were continuously acquired after addition of excess KO_2 (60 µM) using spectramax. The chemiluminescence intensities were plotted as a function of time.

Tissue-penetration studies. MRP$_D$ solution (30 µM) in PBS (10 mM, pH 7.4) was placed in a black 96-well plate. Chicken tissues with the desired thickness were overlaid on top of the wells. Chemiluminescence images were acquired after addition of KO_2 (60 µM) using the IVIS spectrum imaging system under bioluminescence mode with open filter and the acquisition time of 180 s. Fluorescence images were acquired with excitation at 640 ± 10 nm

and emission at 760 ± 10 nm and the acquisition time of 0.1 s. The signal to background ratio (SBR) was calculated as SBR = fluorescence intensities (or chemiluminescence intensities)/background, where background is the signal intensity of neighboring tissues obtained over the imaging period[49]. The SBRs were plotted as a function of tissue depth.

***In vivo* biodistribution studies.** All animal studies were performed in compliance with the guidelines set by the Institutional Animal Care and Use Committee (IACUC), Sing Health. Female nude mice (Tac:Cr:(NCr)-Fox1nu, 8 weeks old) and Balb/c mice (10 weeks old) were purchased from InVivos Pte Ltd (Singapore). Aged female nude mice (25 weeks old) were obtained by feeding after receive at 8 weeks old. NCr nude mice were i.v. injected with 0.2 ml saline (control), the uncaged fluorophores (CMe, CP2, CP5 and CCD, 8 µmol kg^{-1} body weight) or MRP$_D$ (32 µmol kg^{-1} body weight), and imaged using the IVIS spectrum imaging system at 30 and 60 min post-injection. The abdominal cavity and resected organs from mice were imaged after sacrifice at 60 min post-injection. Fluorescence images were acquired using the IVIS spectrum imaging system with excitation at 675 ± 10 nm (640 ± 10 nm for MRP$_D$) and emission at 720 ± 10 nm (760 ± 10 nm for MRP$_D$).

Pharmacokinetic studies. NCr nude mice were anesthetized by i.p. injection of ketamine/xylazine (ketamine: 50 mg kg^{-1} body weight ; xylazine: 5 mg kg^{-1} body weight) for the entire duration of the experiment. The end of the tail was cut for blood extraction. Blood was sampled in heparinized capillary tubes as a reference before injection. Mice were i.v. injected with the uncaged fluorophores (CP2, CP5 and CCD, 8 µmol kg^{-1} body weight), MRPs1-3 (8 µmol kg^{-1} body weight) or MRP$_D$ (32 µmol kg^{-1} body weight) and blood was sampled at 1, 4, 9, 16, 25, 35, 55 and 75 min post-injection. For pharmacokinetic studies of MRPs1-3 and MRP$_D$ in cisplatin-treated mice, blood was sampled from living mice after 1, 4, 9, 16, 25, 35, 55, 75, 95 and 120 min injection of MRPs1-3 (8 µmol kg^{-1} body weight) or MRP$_D$ (32 µmol kg^{-1} body weight) at different timepoints post-treatment of cisplatin (8, 12, 16, 48 or 72 h). Collected blood samples were stored in an ice box to prevent clotting before centrifugation at 3500 r.p.m for 20 min. The uncaged fluorophores and MRPs were quantified using HPLC. Quantification results were presented as a bi-exponential decay curve to estimate elimination ($t_{1/2\beta}$) blood half-life values.

Renal clearance efficiency studies. NCr nude mice were i.v. injected with the uncaged fluorophores (CMe, CP2, CP5 and CCD, 8 µmol kg^{-1} body weight), MRPs1-3 (8 µmol kg^{-1} body weight) or MRP$_D$ (32 µmol kg^{-1} body weight) and placed in metabolic cages. For renal clearance efficiency studies of MRPs1-3 in cisplatin-treated mice, mice were i.v. injected with MRPs1-3 (8 µmol kg^{-1} body weight) at $t = 8$, 12, 16, 48 or 72 h post-treatment of cisplatin (20 mg kg^{-1} body weight) and placed in metabolic cages. Urine was collected at 1, 3, 6, 9 and 24 h post-injection, centrifuged at 4500 r.p.m. for 8 min and filtered by 0.22 µm syringe filter.

Excretion of the uncaged fluorophores and MRPs in the urine was quantified using HPLC. Mice were sacrificed to image resected organs after 24 h urine collection.. Major organs were collected, homogenized in PBS (10 mM, pH 7.4) and centrifuged at 4500 r.p.m for 15 min to remove insoluble components. Fluorescence intensities of the final supernatants were measured on fluorescence spectrophotometer.

***In vivo* stability and biocompatibility studies.** The collected urine in PBS (10 mM, pH 7.4) were measured on UV-Vis and fluorescence spectrophotometer, imaged by the IVIS spectrum imaging system and analyzed by HPLC as well as MALDI-TOF mass spectrometry. Heart, liver, spleen, lung and kidneys were collected from NCr nude mice after 24 h injection of CCD, MRPs1-3 (8 µmol kg^{-1} body weight) or MRP$_D$ (32 µmol kg^{-1} body weight) and placed into 4% paraformaldehyde for histological examination.

Establishment of drug-induced AKI models in living mice. Mice were randomly selected and treated with cisplatin (5 mg kg^{-1}, 10 mg kg^{-1} or 20 mg kg^{-1} body weight, i.p. injection), gentamicin (100 mg kg^{-1} day^{-1}, i.p. injection) or diatrizoate (1000 mg kg^{-1} body weight, i.v injection, water deprivation for 24 h before treatment). The control groups were treated with saline (0.2 ml) or NAC (400 mg kg^{-1} body weight, i.v injection) 30 min prior to cisplatin administration[50]. Body weights of all the mice were recorded during treatment. After drug administration, the weight of mice and signs of discomfort were monitored on a daily basis during the entire experiments (Supplementary **Fig. 36**). Imaging, blood and urine sampling were conducted at different timepoints post-treatment of drug. At the end, mice were euthanized and major organs were placed into 4% paraformaldehyde for histological examination.

Real-time *in vivo* NIRF and chemiluminescence imaging of drug-induced AKI in living mice. Real-time NIRF imaging was conducted every 30 min for 2.5 h after i.v injection of MRPs1-3 (8 µmol kg^{-1} body weight) at t = 8, 12, 16, 24, 48 or 60 h post-treatment of cisplatin, or i.v. injection of MRPs1-2 (8 µmol kg^{-1} body weight) at t = 24, 36, 48 or 72 h post-treatment of gentamicin, or i.v. injection of MRPs1-2 (8 µmol kg^{-1} body weight) at t = 2, 8, 16 or 48 h post-treatment of diatrizoate. Real-time dual-channel imaging was conducted every 30 min for 2 h after i.v injection of MRP$_D$ (32 µmol kg^{-1} body weight) at t = 8, 12, 48 or 72 h post-treatment of cisplatin, or at t = 24, 36, 96 or 144 h post-treatment of gentamicin, or at t = 2, 8, 16 or 48 h post-treatment of diatrizoate. The control groups were treated with saline (0.2 ml), and the negative control was treated NAC (400 mg kg^{-1} body weight, i.v injection) 30 min prior to cisplatin administration. Fluorescence images were acquired using the IVIS spectrum imaging system with excitation at 675 ± 10 nm (640 ± 10 nm for MRP$_D$) and emission at 720 ± 10 nm (760 ± 10 nm for MRP$_D$) and the acquisition time of 0.1 s. Chemiluminescence images were acquired under bioluminescence mode with open filter and the acquisition time

of 180 s. Mice were euthanized after i.v injection of MRPs1-3 or MRPD at different timepoints post-treatment of saline or drugs. The abdominal cavity and resected organs from mice were imaged after sacrifice. Major organs were placed into 4% paraformaldehyde for histological examination.

Determination of GFR in drug-treated living mice[51]. FITC-inulin (150 mg) was dissolved in 0.9% NaCl (3 ml) at 75 °C and dialyzed in 0.9% NaCl (1000 ml) at 25 °C for 24 h. Dialyzed FITC-inulin (3.74 µl g^{-1} body weight)[51] was injected intravenously in living NCr nude mice at t = 8, 12, 16, 24, or 48 h post-treatment of cisplatin (20 mg kg^{-1} body weight), or at t = 24, 36, 48, 96, or 144 h post-treatment of gentamicin (100 mg kg^{-1} day^{-1} body weight), or at t = 2, 8, 16, 24, or 48 h post-treatment of diatrizoate (1000 mg kg^{-1} body weight), or saline (0.2 ml) treated mice. Blood (approximately 20 µl) was collected via saphenous vein at 3, 7, 10, 15, 35, 55, and 75 min post-injection of FITC-inulin, and then centrifuged for 20 min at 3500 r.p.m. Serum sample (10 µl) was diluted with HEPES buffer (40 µl, 500 mM, pH 7.4) and fluorescence was measured using spectramax with excitation at 485 nm and emission at 538 nm. Serum fluorescence data were presented as a two-component exponential decay curve using nonlinear regression. GFR was calculated according to the equation[51]: GFR = I/(A/α + B/β), where I is the amount of FITC-inulin delivered by the bolus injection, A and B are the y-intercept values of the two decay rates, and α and β are the decay constants for the distribution and elimination phases, respectively.

Online urinalysis. Urine was collected from living mice after i.v. injection of MRPs1-3 (8 µmol kg^{-1} body weight) at t = 8, 12, 16, 24, 48 or 60 h post-treatment of cisplatin (10 mg kg^{-1} or 20 mg kg^{-1} body weight), or at t = 24, 36, 48, 72, or 144 h post-treatment of gentamicin (100 mg kg^{-1} day^{-1} body weight), or at t = 2, 8, 16, 24, or 48 h post-treatment of diatrizoate (1000 mg kg^{-1} body weight), or saline (0.2 ml) treated mice. The collected urine samples were centrifuged at 4500 r.p.m. for 8 min, filtered by 0.22 µm syringe filter, and measured on fluorescence spectrophotometer. Fluorescence images were acquired using the IVIS spectrum imaging system with excitation at 675 ± 10 nm and emission at 720 ± 10 nm. Activated MRPs were analyzed by HPLC.

Offline urinalysis. Urine was collected using metabolic cages from drug-treated mice at different timepoints post-treatment of drug. The collected urine samples were centrifuged at 4500 r.p.m. for 8 min and filtered by 0.22 µm syringe filter. MRPs1-3 solutions (30 µM) in PBS (10 mM, pH 7.4) were incubated with the urine (100 µl) at 37 °C, followed by fluorescence measurements on fluorescence spectrophotometer after 2 h incubation. Urinary TFF3, osteopontin, NGAL, β2-Microglobulin, KIM-1, clusterin levels were quantified using ELISA kits according to the manufacturer's protocol.

Blood analysis. Blood was collected from the tail vein in living NCr nude mice under isoflurane anesthesia at t = 8, 12, 16, 24, or 48 h post-treatment of cisplatin (20 mg kg^{-1} body weight), or at t = 24, 48, 72, 96, or 144 h post-treatment of gentamicin (100 mg kg^{-1} day^{-1} body weight), or at t = 2, 8, 16, 24, or 48 h post-treatment of diatrizoate (1000 mg kg^{-1} body weight), or saline (0.2 ml) treated mice. The collected blood samples were centrifuged for 20 min at 3500 r.p.m. Serum creatinine, BUN and cystatin C were determined using commercial kits according to the manufacturer's protocol.

Specificity studies in living mice with local skin inflammation. NCr nude mice were intradermally injected with saline (15 µl) or LPS (5 µg in 15 µl PBS) on the left thigh[52], followed by i.v injection of MRP2 (8 µmol kg^{-1} body weight) at 4 h post-treatment of saline or LPS. Real-time NIRF imaging of living mice was conducted using the IVIS spectrum imaging system. Urine was collected from a separate set of saline or LPS-treated mice at 4 h post-treatment. The collected urine samples were centrifuged at 4500 r.p.m. for 8 min and filtered by 0.22 µm syringe filter. MRP2 solutions (30 µM) in PBS (10 mM, pH 7.4) were incubated with the urine (100 µl) at 37 °C, followed by fluorescence measurement after 2 h incubation. Sections of skin from the injection sites were resected after euthanasia for immunofluorescence staining. Note that such a low dosage of LPS does not induce organ injury[53].

Specificity studies in living mice with ANIT-induced liver injury. NCr nude mice were fasted overnight and intragastrically injected with olive oil (0.2 ml, control group) or ANIT (dissolved in olive oil, 75 mg kg^{-1} body weight)[24], followed by i.v injection of MRPs1-3 (8 µmol kg^{-1} body weight) at 24 h or 48 h post-treatment of olive oil or ANIT. Real-time NIRF imaging of living mice was conducted using the IVIS spectrum imaging system. For online urinalysis, urine was collected from control or ANIT-treated living mice after i.v injection of MRPs1-3 (8 µmol kg^{-1} body weight) at 48 h post-treatment of ANIT. For offline urinalysis, urine was collected from a separate set of control or ANIT-treated mice at 48 h post-treatment. The collected urine samples were centrifuged at 4500 r.p.m. for 8 min and filtered by 0.22 µm syringe filter. MRPs1-3 solutions (30 µM) in PBS (10 mM, pH 7.4) were incubated with the urine (100 µl) at 37 °C, followed by fluorescence measurement after 2 h incubation. Liver and kidneys were resected after euthanasia at 24 h or 48 h post-treatment of olive oil or ANIT for H&E and immunofluorescence staining. Note that ANIT does not induce kidney injury[24].

Histology. All tissues were fixed with 4% paraformaldehyde, dehydrated in a series of ethanol solution, embedded in paraffin and cut into sections with a thickness of 10 µm for H&E staining. The paraffin was removed by xylene washing and then the sections were incubated with hematoxylin for 4 min and eosin for 2 min, followed by washing with distilled

water. The stained sections were examined using a Nikon ECLIPSE 80i microscope. For immunofluorescence staining, liver, heart, lung, skin, spleen and kidney tissues were fixed with 4% paraformaldehyde, dehydrated using 30% sucrose solution, embedded in frozen optimal cutting temperature (O.C.T.) medium, and then cut into sections with a thickness of 10 μm (40 μm for the whole kidney sections). The sections were dried at 25 °C for 60 min, washed three times using PBS containing 0.1% Triton X-100, and incubation with 3% BSA solution at 25 °C for additional 60 min, followed by washing with PBS. The sections were then incubated with respective antibody (cleaved-caspase-3 antibody, anti-CD31 antibody, or anti-CD11b antibody) for 60 min at 37°C. After being washed three times with PBS to remove unbound antibody, the sections were counterstained with Alexa Fluor 488 conjugated goat anti-rabbit IgG H&L for 60 min at 25 °C. Next, the cell nuclei were stained with DAPI. The stained sections were imaged using a LSM800 confocal laser scanning microscope.

Statistics and reproducibility. The in vivo and ex vivo fluorescence or chemiluminescence signals were quantified with ROI analysis using Living Image 4.3 Software. Data are mean ± standard deviation (S.D.) unless stated otherwise. Investigators were blinded to group allocation during experiments. Investigators performing in vivo imaging were blinded to saline and drug treatment groups. Statistical differences between two groups were tested with a two-tailed Student's t-test and more than three groups were determined by one-way analysis of variance followed by Tukey's post hoc test. For all tests, P values less than 0.05 were considered statistically significant. $*P < 0.05$, $**P < 0.01$ and $***P < 0.001$. All statistical calculations were performed using GraphPad Prism 6.0, including assumptions of tests used.

Data availability. The authors declare that all relevant data supporting the findings of this study are available within the article and in the Supplementary Information document, or from the corresponding author on reasonable request.

References

46. Hu, J.J. *et al*. Fluorescent probe HKSOX-1 for imaging and detection of endogenous superoxide in live cells and in vivo. *J. Am. Chem. Soc.* **137**, 6837-6843 (2015).
47. Gu, K. *et al*. Real-time tracking and in vivo visualization of beta-galactosidase activity in colorectal tumor with a ratiometric near-infrared fluorescent probe. *J. Am. Chem. Soc.* **138**, 5334-5340 (2016).
48. Benson, R.C. & Kues, H.A. Absorption and fluorescence properties of cyanine dyes. *J. Chem. Eng. Data* **22**, 379-383 (1977).
49. Hyun, H. *et al*. Structure-inherent targeting of near-infrared fluorophores for parathyroid and thyroid gland imaging. *Nat. Med.* **21**, 192-197 (2015).

50. Dickey, D.T. *et al.* Effect of N-acetylcysteine route of administration on chemoprotection against cisplatin-induced toxicity in rat models. *Cancer Chemother. Pharmacol.* **62**, 235-241 (2008).

51. Qi, Z. *et al.* Serial determination of glomerular filtration rate in conscious mice using FITC-inulin clearance. *Am. J. Physiol. Renal. Physiol.* **286**, F590-596 (2004).

52. Medicherla, S. *et al.* Topical alpha-selective p38 MAP kinase inhibition reduces acute skin inflammation in guinea pig. *J. Inflamm. Res.* **3**, 9-16 (2010).

53. Wang, W. *et al.* Prostacyclin in endotoxemia-induced acute kidney injury: cyclooxygenase inhibition and renal prostacyclin synthase transgenic mice. *Am. J. Physiol. Renal. Physiol.* **293**, F1131-1136 (2007).